Alexandrov RESEARCH INSTITUTE OF TECHNOLOGY
NITI

Phase diagrams for multicomponent systems containing corium and products of its interaction with NPP materials

(CORPHAD)

Phase 2

Investigation of ternary systems:

The U-Fe-O system

PROGRESS REPORT
01/05/06 – 30/11/06

Project title	Phase diagrams for multicomponent systems containing corium and products of its interaction with NPP materials (CORPHAD, 1950.2)	
Commissioned by	ISTC	
File specification	CORPHAD/RCP-0601	
Implementing organization	The Alexandrov Research Institute of Technology (NITI) of the Atomic Energy Agency of the Russian Federation	
Project manager	Name	Yu. N. Aniskevich
	Signature	
	Date	November, 2006

Authors

Dr., Prof.	V. B. Khabensky
Dr.	S. V. Bechta
Ph.D.	V. S. Granovsky
Dr., Corr.Mem. RAS	V. V. Gusarov
	V. I. Almyashev
	S. A. Vitol
	E. V. Krushinov
Dr., Prof.	Yu. B. Petrov
Ph.D.	S. Yu. Kotova
Ph.D.	A.A. Sulatsky
Ph. D.	I. V. Kulagin
Ph. D.	D. B. Lopukh
Ph.D.	L. P. Mezentseva
	E. K. Kalyago
	V. V. Martynov
	A. V. Lysenko
	R. A. Kosarevsky
	E. V. Shevchenko
	V. G. Bliznyuk
	V. R. Bulygin
	E. M. Belyaeva
	N. E. Kamensky

CONTENTS

INTRODUCTION

The present work has been carried out within the ISTC CORPHAD Project in order to specify phase diagrams of corium-based systems and products of its interaction with NPP materials. The availability of credible information about phase equilibria in such systems is very important for a consistent prediction of physicochemical phenomena taking place in a faulty nuclear reactor during the core heatup and meltdown, molten pool formation and evolution, as well as also in the cases of melt interaction with materials limiting its attitude position.

The metal-oxidic system U–Fe-O is one of the basic systems essential for the reliable determination of phase ratios during the in-vessel retention of corium. Due to an extremely high chemical activity of melts in the concentration domain of interest, such systems can be investigated only in a neutral atmosphere or in the atmosphere with regulated partial pressure of oxygen. In addition to the mentioned peculiarity, this system is prone to stratification /1/, as is shown by the available data on binary diagrams, and by thermodynamic calculations. The published sources contain no experimental data for the diagram concentration domain of interest. These circumstances considerably complicate methodologies of melt preparation, manipulation and investigation.

The present work was aimed at the experimental evaluation of liquidus and solidus temperatures (T_{liq} and T_{sol}) for the compositions recommended by the CORPHAD collaborators, and at identifying compositions of the liquids that coexist in the miscibility gap.

1. Publications review

Below one can find modern versions of phase diagrams of 3 binary systems (Figs. 1.1-1.4) that form the ternary system in question.

Diagrams of just 2 types are given for the U-O system, though the number of published ones is much greater. Fig. 1.1 shows a phase diagram for the U-UO_2 system constructed by Edwards and Martin /2/.

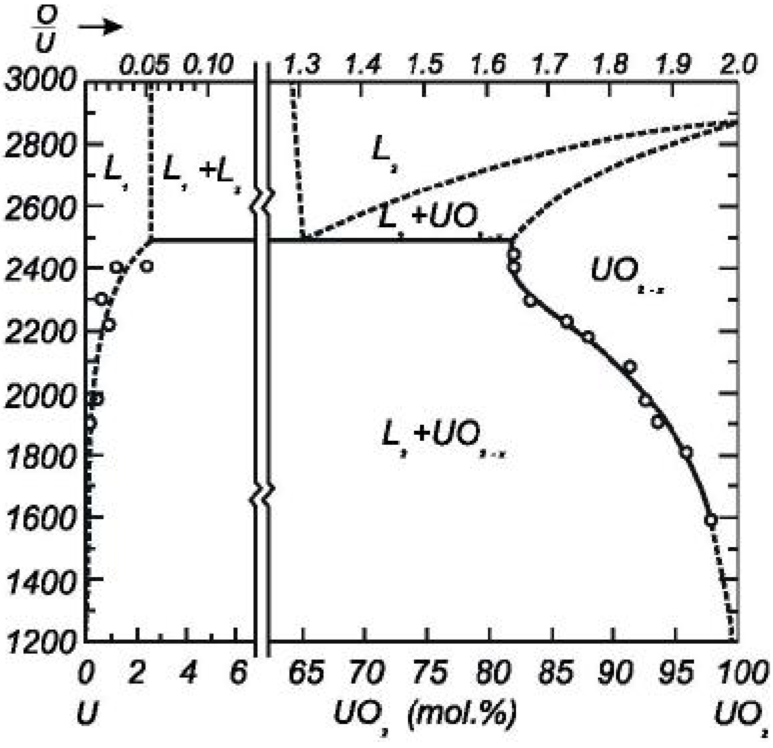

Fig. 1.1. Phase diagram of the U-UO$_2$ system according to /2/.

His diagram is peculiar because of the area of nonstoichiometric UO$_{2-x}$ that widens with the growth of temperature, and the area of liquids immiscibility. A very low solubility of oxygen in liquid uranium attracts attention: for example, it is about 4 at.% at 2500° C.

The second version of a phase diagram of the U-UO$_2$ system (Fig. 1.2), constructed on the basis of the data from Guinet et al /3/, practically coincides with the above-considered diagram concerning the area of nonstoichiometric UO$_{2-x}$ existence, but differs from it by a high solubility of O in liquid U (up to 40 at. % at 2300° C.

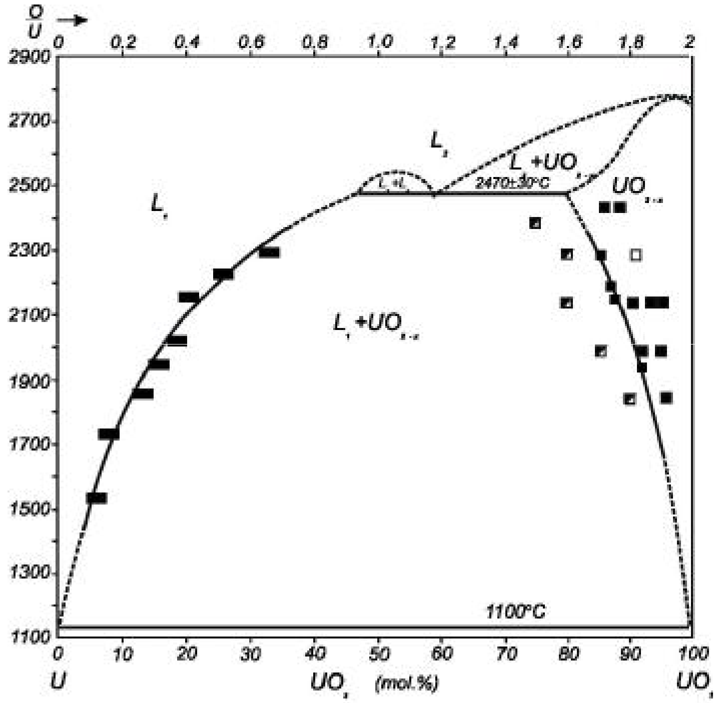

Fig. 1.2. Phase diagram of U-UO$_2$ according to /3/

In the diagram by Edwards and Martin (Fig. 1.1), an extensive gap in miscibility of two liquids (L_1 and L_2) stretches from 2.5 up to 65 mol. % UO_2, and temperaturewise it is over 500 K. The diagram by Guinet et al. (Fig. 1.2) shows the immiscibility gap to be just 12 mol. % UO_2 in terms of concentration, and temperaturewise the authors suppose it to be around 100 K. Significant discrepancies in the experimental data concerning solubility of oxygen in molten uranium are reflected in phase diagrams of the U-UO_2 system as different widths of the immiscibility gap.

The binary diagram of the U–Fe system (Fig. 1.3) has been studied sufficiently long ago. It is characterized by formation of two intermetallic compounds – U_2Fe and U_6Fe, and by the presence of two eutectics. According to the authors of /4/, the first compound melts congruentially at 1235° C, while the second decomposes at 805° C. The shape of the liquidus curve for the diagram area with the concentration of Fe above 12 mass % has not been determined. No mutual solubility of components was observed in the system.

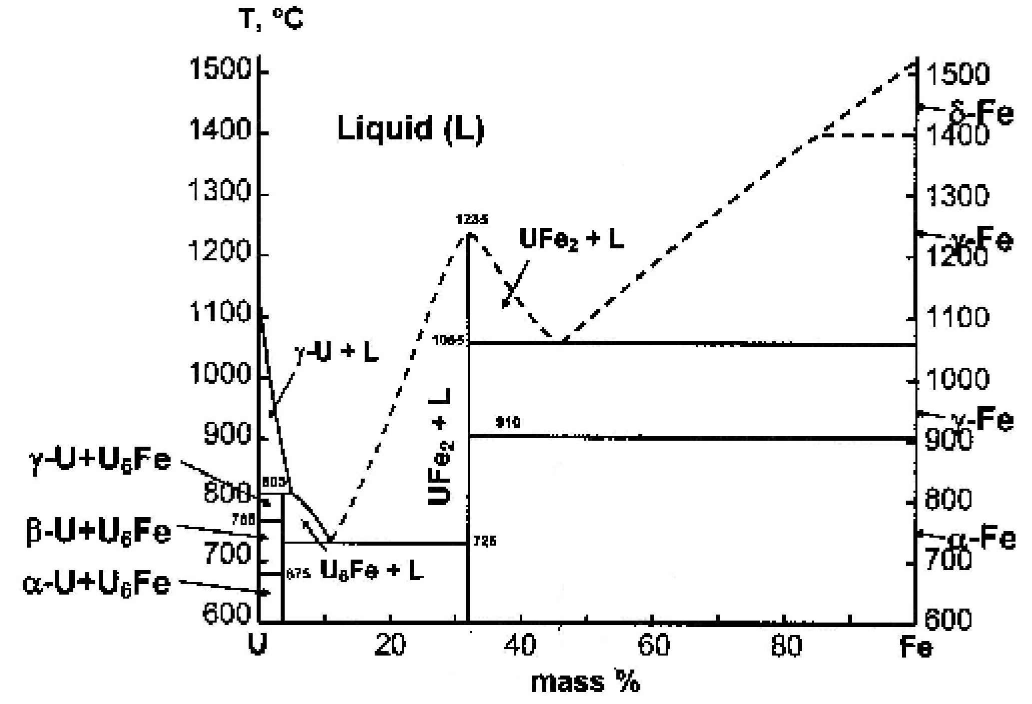

Fig. 1.3. Diagram of the uranium-iron system according to /4/

The binary diagram of the Fe–O system, i.e. of a fundamental one for many metallurgical processes, has been studied sufficiently well. High-temperature equilibria between metallic iron and its oxides have been most comprehensively studied in /5/. The area of stratification stretches from 0.4 up to 50 at. % O (Fig. 1.4). Note the insignificant solubility of oxygen in Fe, which grows with the increasing temperature.

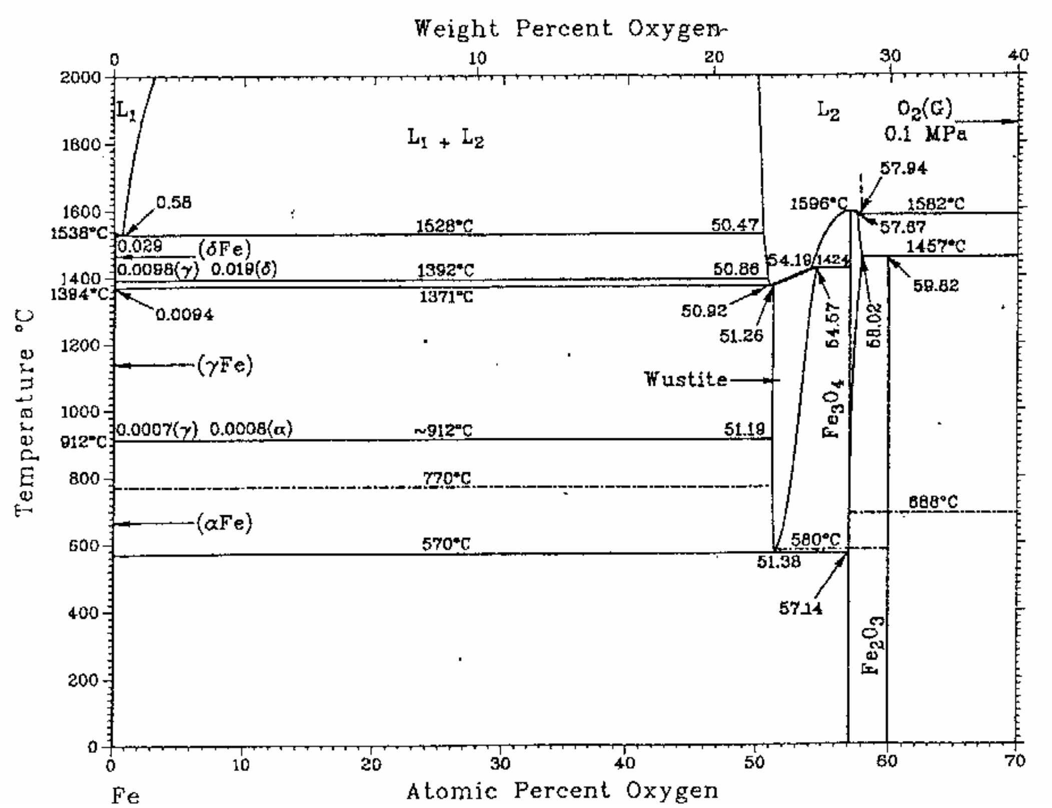

Fig. 1.4. The Fe-O system under 1 atm, according to /5/

The Fe-O system has been studied fairly well and its phase diagram does not raise doubts at the present level of experimental capabilities. At the same time, the diagrams of U-O and U-Fe systems still contain quite a number of uncertainties. Therefore, experimental investigations of the U-Fe-O system are of high importance.

2. Experimental methodologies and description of facilities

Measurements of T_{liq} was performed by means of visual polythermal analysis in the cold crucible (VPA IMCC). Determination of T_{sol} was made by the method of differential thermal analysis (DTA) using the SETARAM analyzer. Compositions of the coexisting liquids were determined using the results of the physicochemical analysis. Descriptions of the facilities and experimental methodologies are given in /6/.

3. Description and results of tests

3.1. Analysis of initial charge materials

When preparing the test, the charge components were checked for the main substance and impurities content, and the O/U ratio in the powdered urania was found to be 2.24 by thermogravimetry /7, 8/.

The composition of charge components is given in Tab. 3.1.

Table. 3.1. Charge components

Components	Main substance content, %	Impurities, mass %	Notes
Fe	Fe>99.9	Si-0.0005; Mg-0.0001; Cu-0.0001; Ni-0.019; Pb-0.0001; Zn-0.00028	Passport data
powdered $UO_{2.24}$, dispersivity < 40 µm	$UO_{2.24}$>99.0	Fe<0.03; As<0.0003; CuO<0.01; phosphates<0.002; chlorides<0.003, ZrO_2<0.9	Passport data, thermogravimetry, XRF
U	U>97.0 U^{238} – 99.72 U^{234} – 0.002 U^{235} – 0.28	Zr<2.7 Fe<0.30	XRF and gamma-spectrometry

It should be noted that the used metallic uranium contained metallic zirconium, and this could affect equilibria in the investigated system.

3.2. Experimental matrix

All in all, 2 tests were made with crucible charge identical in composition. The test CORD40 was a repetition of CORD36 because of the reasons stated below. The crucible charge is given in Tab. 3.2.

Table. 3.2. Crucible charge composition for CORD36 and CORD40

CORD	U	Fe	O	Mass, g
	mass%/at.%			
36	90.9/60	7.1/20	2.0/20	632.7
40				602.0

3.3. Experimental procedures

The experimental procedures for T_{liq} determination were identical and included:

- Charge materials preparation (metal cutting and powders calcination) and their thorough mixing in argon.
- Furnace loading with the specified composition and its blasting with argon.
- Molten pool production and its superheating above T_{liq}.
- Molten pool depth and bottom crust measurement.

- Melt sampling.
- Lifting of the crucible with melt relative to the inductor, thus bringing the molten pool above the inductor upper coil. This causes suppression of the meniscus that is characteristic of the metal-oxidic systems, cooling down of the upper layers of the melt, and solid phase formation at the melt surface.
- Repeated moving of the crucible with melt to a fixed position and videorecording of the films/crusts formation process for T_{liq} determination.
- Heating termination. Pool surface videorecording.
- Ingot extraction from the crucible for the subsequent analysis.

Brief descriptions of the performed tests are given below.

CORD36

After formation of the molten pool, two liquids were observed on its surface. Temperature of the melt surface was measured by the spectral ratio pyrometer RAYTEK MR1-SC. The pyrometer measures both the colour temperature and two brightness temperatures at 0.9 и 1.05 µm wavelengths.

While the colour temperature of the molten pool surface was approximately the same, the brightness temperatures of different liquids varied. This phenomenon made it possible to find the emissivity factor for the “oxidic” and “metallic” liquids (hereinafter used without inverted commas) to be 0.49 and 0.23, respectively. Fig. 3.1 shows the surface of the oxidic, lighter coloured part of the molten pool. The colour temperature was Tc=2618° C and the brightness ones – $T_{\lambda1}$=2199° C and $T_{\lambda2}$=2157° C. Fig. 3.2 presents the surface of the metallic, darker coloured part of the molten pool. The colour temperature was Tc=2651°C and the brightness ones – $T_{\lambda1}$=1947° C and $T_{\lambda2}$=1886° C.

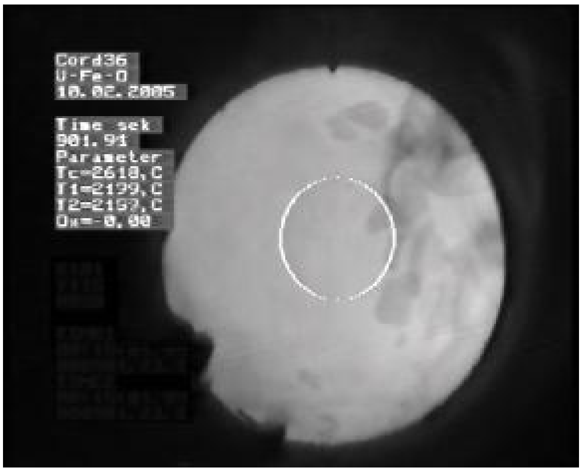

e_l » **0.49**

l_1**=0.9** m**m**

l_2**=1.05** m**m**

Fig. 3.1. Videoframe of the oxidic melt surface

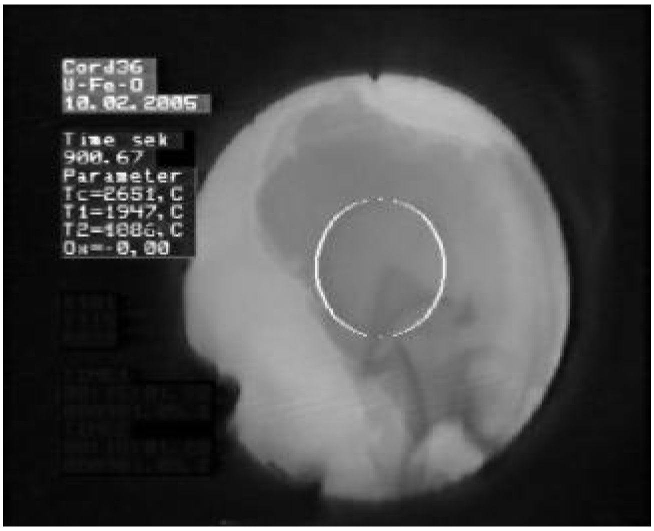

e_l » **0.23**

l_1**=0.9** mm

l_2**=1.05** mm

Fig. 3.2. Videoframe of the metallic melt surface

Electrical characteristics of the high-frequency generator and history of the melt surface temperature throughout the test are given in Fig. 3.3.

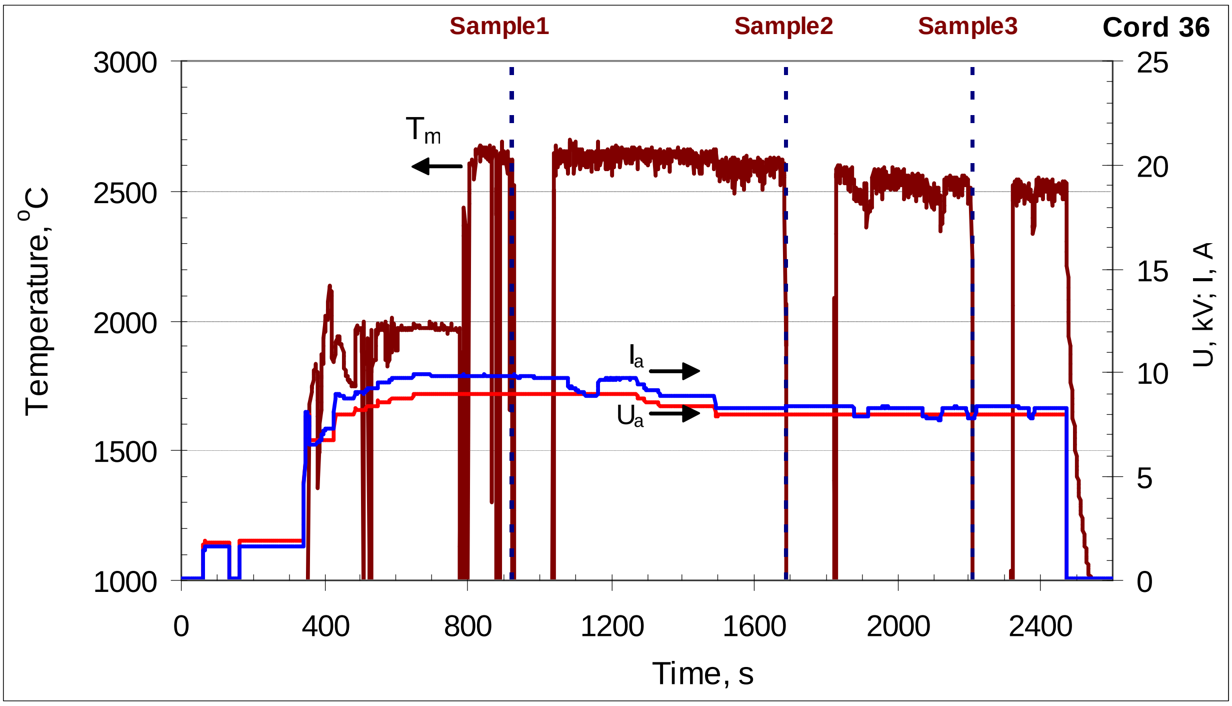

Fig. 3.3. History of the melt surface temperature (Tm), anode current (Ia) and anode voltage (Ua)

During the test, T_{liq} was measured twice by the VPA IMCC method and found to be 2472° C and 2492° C. Fig. 3.4 shows a thermogram with videoframes of the molten pool surface at T_{liq} measuring. The temperature scattering in the diagram is explained by a big amount of aerosols, of iron in particular. Due to the impossibility of blowing aerosols away in the pyrometer sighting area, it is recommended to take the maximum measured value, i.e. 2492° C, as the value of T_{liq}. Three rod samples of the melt were taken during the test. A big amount of vapours and aerosols led to a plasma discharge. This served as a reason for decreasing the anode voltage, which led to the reduction of power in the melt and dropping of the molten pool surface temperature.

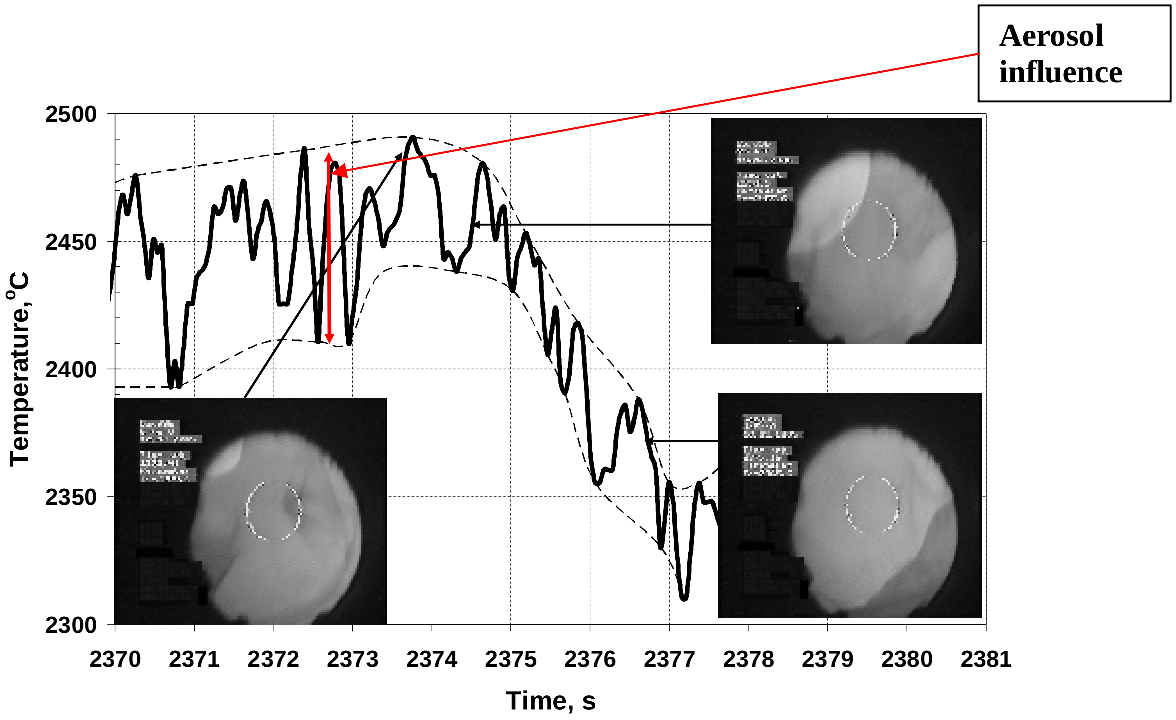

Fig. 3.4. Thermogram with the molten pool surface videoframes

CORD40

After the SEM/EDX examination of the ingot from CORD36 and analysis of thermal processes in the induction system it became obvious that the reduction of power in the melt during the test resulted in crystallization of the refractory phase on the pool bottom. In this relation, it was decided to repeat the test in a way that would minimize its duration and influence on the melt by excluding the pool depth measurements and melt sampling.

Electrical characteristics of the high-frequency generator and history of the melt surface temperature throughout the test are given in Fig. 3.5. As in CORD36, two liquids were observed at the molten pool surface in this test.

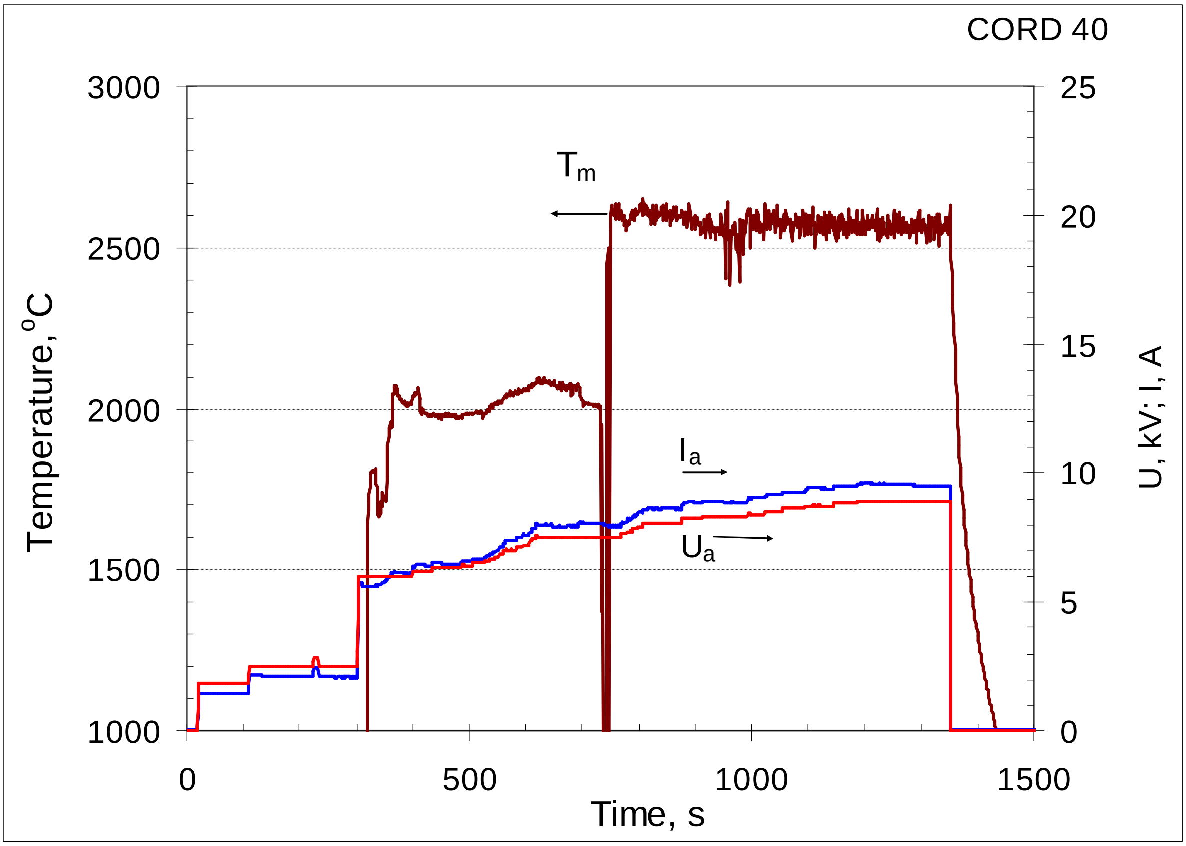

Fig. 3.5. History of the melt surface temperature (Tm), anode current (Ia) and anode voltage (Ua)

T_{liq} was measured once during the test. A thermogram with videoframes of the molten pool surface is presented in Fig. 3.6.

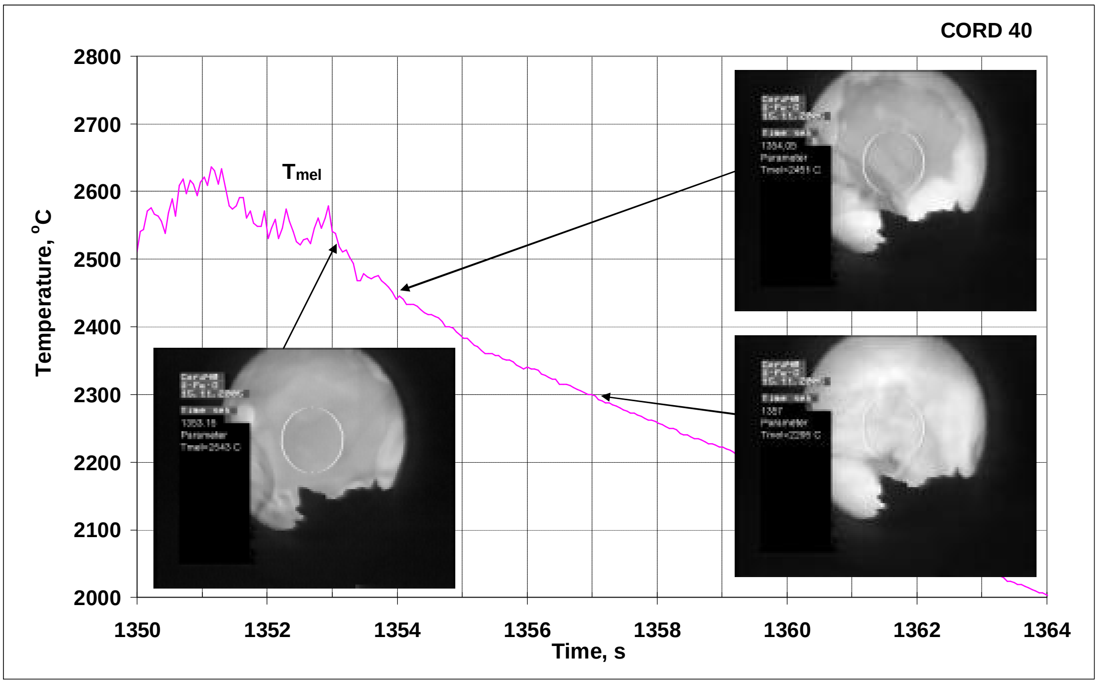

Fig. 3.6. Thermogram with the molten pool surface videoframes

The measured T_{liq} was 2515° C. The fact that this value exceeds the value obtained in CORD36 is obviously due to differences in the molten pool composition.

3.4. Posttest analysis

A number of physicochemical investigations were carried out for determining composition of the liquids coexisting in the melt and for studying the path of crystallization.

3.4.1. Ingots macrostructure

After the tests, the furnaces were disassembled, ingots extracted and cut longitudinally. One half of the ingot was used for making a microsection for SEM/EDX analysis, and from the other one (refers to CORD40 only) samples were taken for XRF, chemical analysis, bottle density determination and oxygen content determination by means of carbothermal reduction (CTR).

Fig. 3.7 shows the longitudinal section of the ingot from CORD36.

Fig. 3.7. Longitudinal section of the ingot from CORD36

In CORD36, there was a UO_2-rich layer at the pool bottom.

In CORD40, the oxidic part was located at the pool surface as a thin layer.

Fig. 3.8 shows the longitudinal section of the ingot from CORD40 and the pattern of sampling for XRF, chemical analysis, bottle density determination and CTR. Figures in the diagram refer to the samples for XRF.

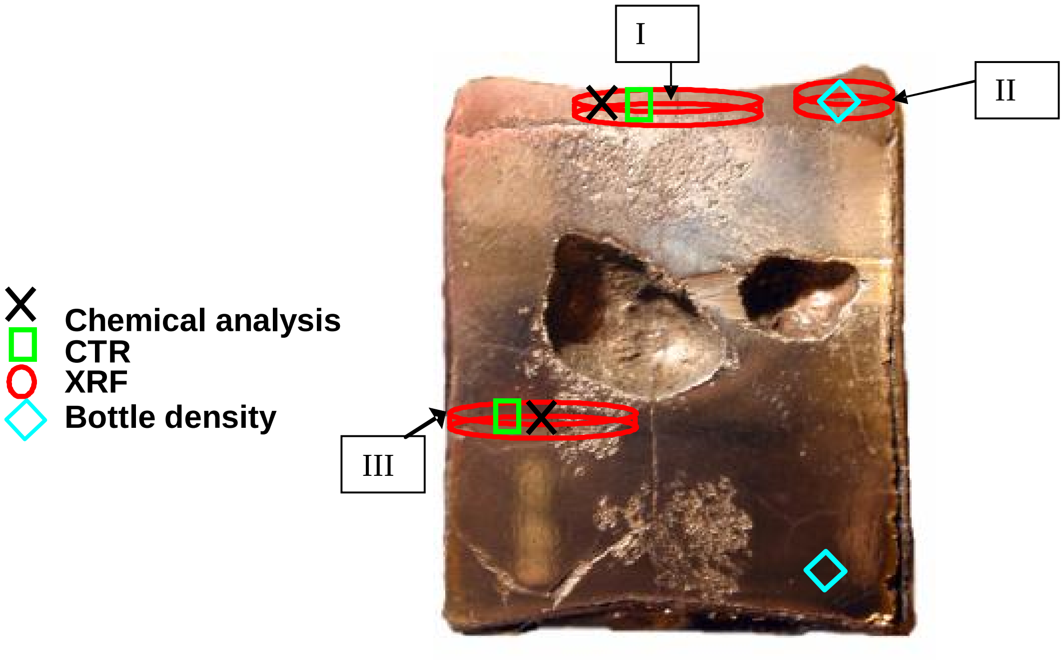

Fig. 3.8. Longitudinal section of the ingot from CORD40 and sampling pattern

3.4.2. Densities of the oxidic and metallic parts of the corium ingot

In order to calculate masses of the oxidic and metallic parts of the ingot with the aim of making up the per-element mass balance, bottle densities were determined for the parts and the volumes were calculated from their areas in the longitudinal section (supposing axial symmetry). Calculations were made using the formula 3.1.

$$m = V \cdot r \qquad (3.1)$$

where m is the mass of the oxidic/metallic part, g;

V is the volume of the oxidic/metallic part, cm^3;

r is bottle density of the oxidic/metallic part, g/cm^3.

Densities of the metallic and oxidic parts were determined according to the technique described in /17/. Locations of samples taking for analytical purposes are shown in Fig.3.8. High-purity ethyl alcohol was used as the liquid for the bottle method.

The bottle density of the metallic part from CORD40 was 15.4 g/cm^3 under normal conditions, and the volume was 34.44 cm^3. The oxidic part had a density of 11.9 g/cm^3 and its volume was 3.33 cm^3.

The bottle density evaluation error was ±2 %.

3.4.3. Material balances of the tests

In order to make up material balances of the tests, the initial charge components and fused products were weighed with accuracy up to 0.1 g.

Material balances of CORD36, 40 are given in Tab. 3.3.

Table. 3.3. Material balances of CORD36, 40

CORD	**Introduced into the melt, g**		**Collected, g**	
36	**UO$_{2.24}$**	98.4	**Ingot**	541.6
	U	489.3	**Corium from probe**	10.3
	Fe	45.0	**Spillages**	7.5
			Rod samples	49.3
			Aerosols	1.3
			Crusts	19.4
	Σ	**632.7**	**Σ**	**629.4**
	Debalance	**3.3**		
40	**U**	465.4	**Ingot**	570.0
	Fe	42.8	**Spillages**	29.9
	UO$_{2.24}$	93.8		
	Σ	**602.0**	**Σ**	**599.9**
	Debalance	**2.1**		

The aerosols collected during CORD40 did not exceed 0.1 g, therefore their mass was not taken into account when making up the material balance. Insignificant values of debalances (0.5 and 0.3%, respectively) confirm representativity of the conducted investigations.

3.4.4. X-ray fluorescence (XRF) analysis

The elemental composition of samples from CORD40 was determined by the XRF method using the SPECTROSCAN MAX-GV /16/. It is evident from Fig. 3.8 that the separation into the oxidic and metallic parts occurred, therefore samples representing flat, ground plates ~ 10×15 mm^2 were cut from the characteristic zones (zones I, II, III) of the ingot. All the works on samples preparation for the analysis were performed in argon.

For analyzing the oxidic part (zones I, II, Fig. 3.8), a technique of compacted pellets was applied to the preparations. Two-layer pellets composed of a mixture of uranium and iron oxides taken in different proportions were fused by the IMCC method in a small crucible to serve as calibration samples. The results of analyzing the ingot oxidic part (zones I, II) can be found in Tab. 3.4.

Quantitative analysis of the metallic part (zone III, Fig. 3.8) employed the method of fundamental parameters (MFP), the choice of which is explained in the first place by the absence of calibration (standard) specimens. The method is based on the use of theoretical dependences that describe physical processes of X-ray fluorescence excitation in a sample and subsequent registration of this radiation by spectrometer. This method allows calculation of concentrations of virtually any set of the determinable elements in the studied sample without the use of any comparative (calibration) specimens. In this case, the total elements resulting from calculation of the main elements content should make 100%. Accuracy of the standards-free analysis of alloys and simple mixtures reaches 5 relative %. According to the results of CTR analysis, the content of oxygen in the metallic part of the ingot (zone III) was 0.8±0.07 mass % (see Tab. 3.28). The spectrometer-nonidentifiable oxygen was specified according to the CTR results, and then the total elements were taken as 100% in calculations. Tab. 3.4, zone III-I, contains the XRF data for the metallic part obtained by MFP. Analysis of the data has shown differences in the cationic composition in comparison with the results of EDX and chemical analyses. In order to specify the composition, the metallic plate was fully oxidized (zone III, Fig.3.8). The sample was oxidized within 3 hours by heating it up to 1100º C in air, and then crushed in the vibrating mill down to particles sized <50 μm. The powder was pressed into a pellet and analyzed by the SPECTROSCAN MAX-GV spectrometer using oxidic calibration specimens. Tab. 3.4, zones III-II, offers the XRF data for the oxidized metallic part, and for zone III these data were renormalized taking the oxygen determined by CTR into account.

Table. 3.4. XRF data for samples from CORD40

Sample	Content, mass %				Content, at.%			
	U	Fe	Zr	O[1]	U	Fe	Zr	O
Zone I[2] (without globules)	88.2	0.8	3.0	8.0	40.4	1.6	3.5	54.5
Zone I[2] (with globules[3])	86.6	2.8	2.6	8.0	38.6	5.3	3.0	53.1
Zone I, average	87.4	1.8	2.8	8.0	39.5	3.5	3.3	53.8
Zone II[2]	87.5	1.9	2.6	8.0	39.5	3.6	3.1	53.8
Zone III-I	89.6	8.0	1.6	0.8	64.1	24.4	3.0	8.5
Zone III-II[4]	77.1	6.5	2.0	14.4[5]	23.8	8.5	1.6	66.1
Zone III	89.3	7.6	2.3	0.8	64.2	23.0	4.3	8.6

[1] – oxygen was specified according to the results of CTR analysis.
[2] – see Fig. 3.8.
[3] – see Fig. 3.24, region 5-1-2 and Tab. 3.21, SQ3.
[4] – oxidized metallic part.
[5] – determined from residue.

It is evident from Tab. 3.4 that the distribution of iron in the oxidic part is nonuniform both along the ingot height and radius.

To make up the per-element material balance (see Tab. 3.5) for the metallic part, the normalized data from the 'Zone III' line were taken. The averaged results of Zone I analysis were taken as the data for the oxidic part.

Table 3.5. Elemental material balance for CORD40 according to XRF data

Element	Introduced, g[1]	Mass of the ingot oxidic part[2], g/ density, g/cm^3	Mass of the ingot metallic part[2], g/ density, g/cm^3	Collected, g			D, g
				Oxidic part, g	Metallic part, g	Total, g	
U	506.06	39.6/11.9	530.4/15.4	34.93	473.65	508.57	+2.51
Fe	42.80			0.32	40.31	40.63	-2.17
Zr	12.98			1.19	12.20	13.39	+0.41
O	8.16			3.17	4.24	7.41	-0.75

[1] – introduced into the melt, the spillages (m=29.9 g) and debalance (m=2.1 g) included.
[2] – masses of the oxidic and metallic parts were calculated on the basis of their densities and volumes (see Sect. 3.4.2).

The uranium and iron debalance (see Tab. 3.5) is approximately ±2.5 g. This sufficiently small quantity determined by errors of determining masses of the oxidic and metallic parts of the ingot (±10 g) and by the procedural error.

The error of determining the content of U, Zr and Fe by XRF was 5 relative %.

3.4.5. Chemical analysis

The melt rod samples from CORD36 and the samples prepared from the ingot from CORD40 were analyzed for the content of U and Fe.

The rod samples from CORD36 were separated into two parts (see Fig. 3.9), the top and bottom ones. Then each of them was crushed down to particles sized 100 µm, quartered, and further ground into particles sized no more than 50 µm.

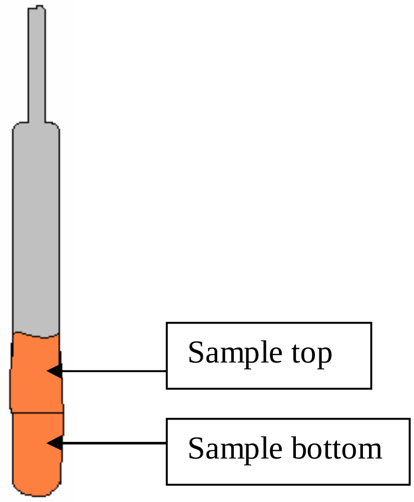

Fig. 3.9. Principle of rod samples preparation for chemical analysis (CORD36)

The ground corium batch of 0.1 g was dissolved in a mixture of concentrated orthophosphoric and sulphuric acids (1:2) in argon, and then the determination of iron content was done by photocolorimetry with orthophenanthroline /9, 10/, while that of uranium – with arsenazo III /11, 12/.

Small pieces up to 0.5 g were chosen for chemical analysis from both bottom and top parts of the ingot from CORD40 (see Fig. 3.8).. All the works on samples preparation for the analysis were performed in argon.

For the samples from CORD40 a new analytical technique has been applied. It made it possible 1) to increase the studied sample mass, and 2) to avoid the laborous preliminary sample grinding down to 50 µm. The 0.1 - 0.5 g samples chosen from the ingot were fused with (3.0±0.5) g of potassium pyrosulfate at 900±25° C until obtaining a transparent fusion cake, which was later dissolved in 200 – 250 ml 1M solution of sulphuric acid. Then the determination of iron content was done by photocolorimetry with orthophenanthroline /9, 10/, of that of zirconium – with xylenol orange / 13, 14, 15/, and of uranium – with arsenazo III /11, 12/.

Tab. 3.6 presents the results of chemical analysis of the samples from CORD36, 40.

Table 3.6. Results of chemical analysis for CORD36, 40

CORD	Sample	Content, mass%				Content, at.%			
		U	Fe	Zr	O[2]	U	Fe	Zr	O
36[1]	Rod sample 1(top)	88.2	10.0	-	1.8	56.0	27.0	-	17.0
	Rod sample 1 (bottom)	74.7	23.9	-	1.4	37.8	51.6	-	10.6
	Rod sample 2 (top)	85.9	13.0	-	1.1	54.5	35.1	-	10.4
	Rod sample 2 (bottom)	76.9	21.4	-	1.7	39.8	47.2	-	13.0
	Rod sample 3 (top)	85.8	14.0	-	0.2	57.8	40.2	-	2.0
	Rod sample 3 (bottom)	81.7	15.8	-	2.5	43.9	36.2	-	19.9
40	Ingot (oxidic part)	92.3	1.0	2.0	4.7	53.8	2.5	3.0	40.7
	Ingot (oxidic part)[3] *with correction for oxygen*	89.1	1.0	1.9	8.0	41.0	2.0	2.3	54.8
	Ingot (metallic part)	89.6	7.7	2.1	0.6	65.5	24.0	4.0	6.5
	Ingot (metallic part)[3] *with correction for oxygen*	89.4	7.7	2.1	0.8	64.0	23.5	3.9	8.5
	Zone III[4]	U^{+4}= 33.4; U^{+6}= 42.9	Fe^{+2}= 6.0	not identified	17.7 (incl. Zr)	-	-	-	-

[1] –Zr was not analyzed

[2] -O determined from the residue

[3] – oxygen specified according to the results of CTR analysis, and data on the main elements renormalized.

[4] – oxidized metallic part.

The oxidized metallic plate (zone III, Fig. 3.8) has also been subjected to chemical analysis in order to determine the final degree of uranium oxidation after oxidation of the sample, and to confirm reliability of the XRF results.

To make up the per-element material balance (Table 3.7) the data for the oxidic and metallic parts were used, to which a correction for oxygen had been applied taking into account the results of CTR (see Sect. 3.6).

Table 3.7. Per-element material balance for CORD40 according to chemical analysis

Element	Introduced, g[1]	Mass of the ingot oxidic part[2], g/ density, g/cm^3	Mass of the ingot metallic part[2], g/ density, g/cm^3	Collected, g			D, g
				Oxidic part, g	Metallic part, g	Total, g	
U	506.06	39.6/11.9	530.4/15.4	35.29	474.33	509.62	+3.55
Fe	42.80			0.38	40.76	41.15	-1.65
Zr	12.98			0.76	11.12	11.88	-1.10
O	8.16			3.17	4.19	7.36	-0.80

[1] – introduced into the melt, the spillages (m=29.9 g) and debalance (m=2.1 g) excluded.

[2] – masses of the oxidic and metallic parts were calculated on the basis of their densities and volumes (see Sect. 3.4.2).

It is evident from Tab. 3.7 that concerning the main elements, debalance does not exceed 3 g.

The error of U determination by photocolorimetry was 5 relative %, and that for Zr and Fe – 3 relative %.

3.5. SEM/EDX analysis

Microstructure and elemental composition of the samples were studied by means of scanning electron microscopy (SEM) and energy dispersive X-ray spectrometry (EDX).

The SEM study employed the ABT-55 scanning electron microscope, and the OxfordLink microprobe attachment was used for the elemental analysis of the samples' regions marked for examination.

The spectral characteristic was taken for each sample for determining its integral composition and that for each separate phase. The quantitative analysis was made by comparing spectral intensity of the reference (superpure, specially prepared substances) and studied samples. The used references of U, Zr, Cr, Fe, Si, Ca, Ni were a part of the Link microprobe attachment set.

The threshold of reliable element identification depends on its sequential number in the Mendeleyev's periodic table and varies from 0.3 to 0.5 mass %. Detection of smaller quantities of elements is unreliable.

The EDX analyzer of the ABT-55 microscope is insensitive to light elements (to oxygen, for instance), therefore the quantity of oxygen was determined with this instrument from the mass deficiency and the error was ~5 mass %.

After the tests, the ingots were cut along the axis, and polished sections were produced from the halves or quarters. Melt samples represented 0.5 – 1.0 mm-thick plates quenched on the massive rod cold surface. Thin sections were prepared from cross-sections of the plates. Then thin sections were examined by SEM and the coexisting phases analyzed.

CORD36

The results of SEM/EDX analysis of rod samples from this test are given in Figs. 3.10-3.12 and in Tabs. 3.8-3.10. The ingot itself with the regions marked for SEM/EDX analysis is shown in Fig. 3.13, while the marked regions and the SEM/EDX results are presented in Figs. 3.14-3.18 and in Tabs. 3.11-3.15.

All samples have a fine-grained structure characteristic of the conditions of fast quenching. A small amount of rounded darker inclusions has been noticed in the microstructure of sample 1 (Fig. 3.10, region 1-1), and this can be an evidence of the melt stratification. The presence of two liquids were visible in the course of the test. The existence of two liquids is confirmed by the differences in bulk composition of regions (Table 3.8).

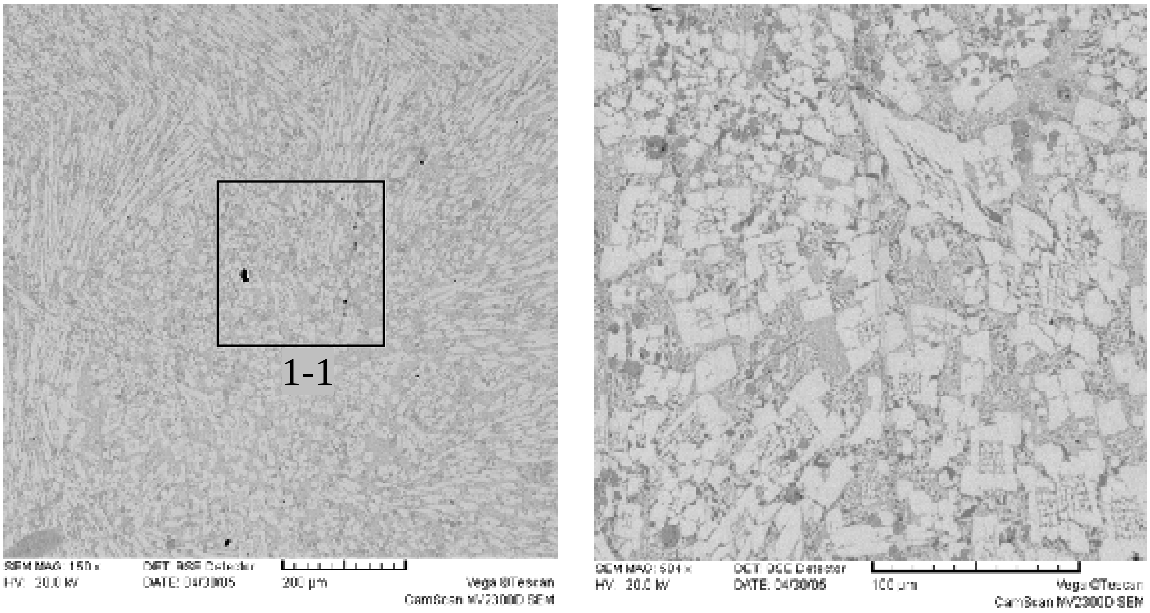

1 (SQ1) 1-1

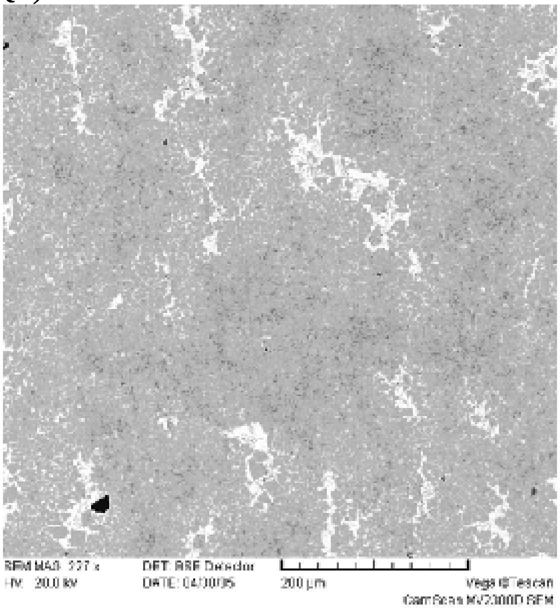

2 (SQ2)

Fig. 3.10. Micrographs of specimens selected from sample No.1, CORD 36

Table 3.8. EDX data for specimens selected from sample No.1

No.		U	Zr	Fe	O
SQ1 top	mass%	87.02	1.13	9.55	2.30
	mol.%	52.78	1.79	24.68	20.75
	mol.%	66.60	2.26	31.15	
SQ2 bottom	mass%	67.59	0.77	30.00	1.64
	mol.%	30.46	0.91	57.63	11.00
	mol.%	34.23	1.02	64.75	

The presence of Zr is explained by its presence in the initial U reagent.

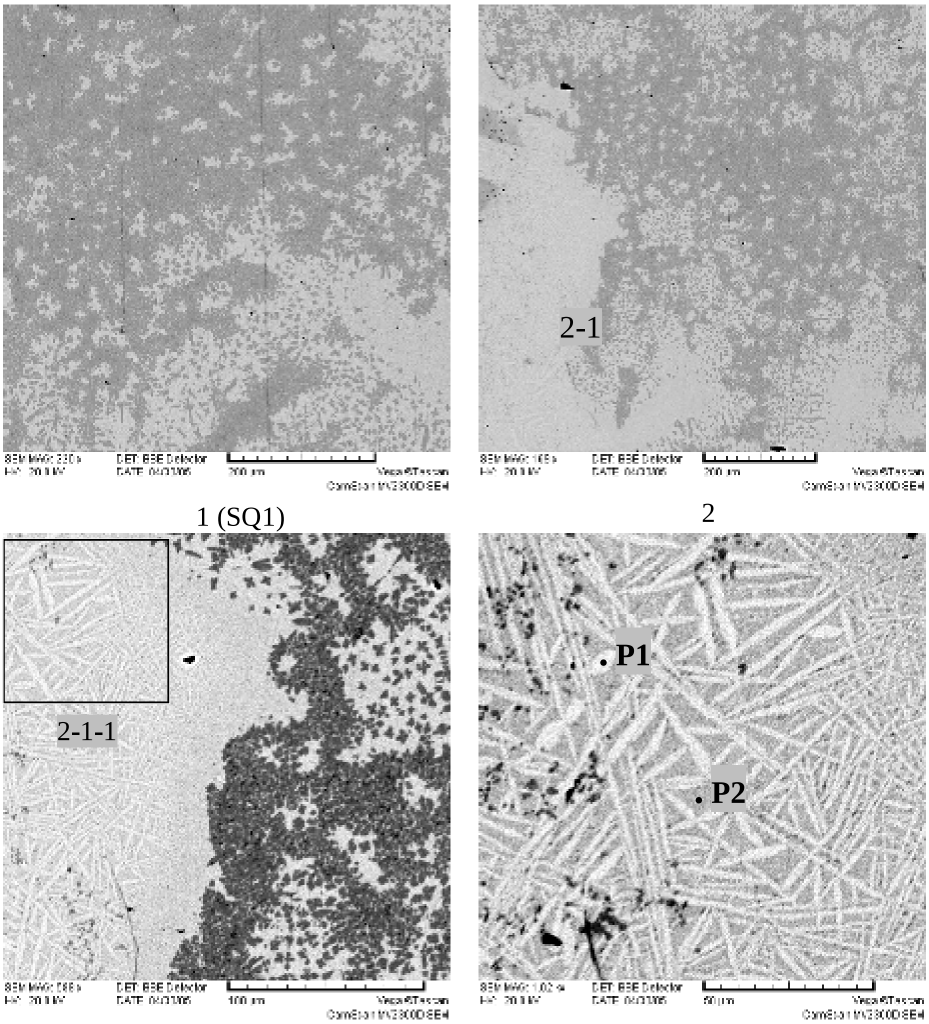

1 (SQ1) 2

2-1 2-1-1 (SQ2)

Fig. 3.11. Micrographs of specimens selected from sample No.2, CORD 36

Table 3.9. EDX data for specimens selected from sample No.2

No.		U	Zr	Fe	O
SQ1 top	mass%	73.69	0.79	23.77	1.75
	mol.%	36.28	1.01	49.89	12.82
	mol.%	41.61	1.16	57.22	
SQ2 bottom	mass%	87.58	0.75	10.01	1.66
	mol.%	55.82	1.25	27.19	15.74
	mol.%	66.25	1.48	32.27	
P1	mass%	90.76	1.13	6.93	1.18
	mol.%	64.46	2.09	20.98	12.47
	mol.%	73.64	2.39	23.97	
P2	mass%	85.47	0.87	12.35	1.31
	mol.%	53.46	1.42	32.93	12.19
	mol.%	60.89	1.62	37.5	

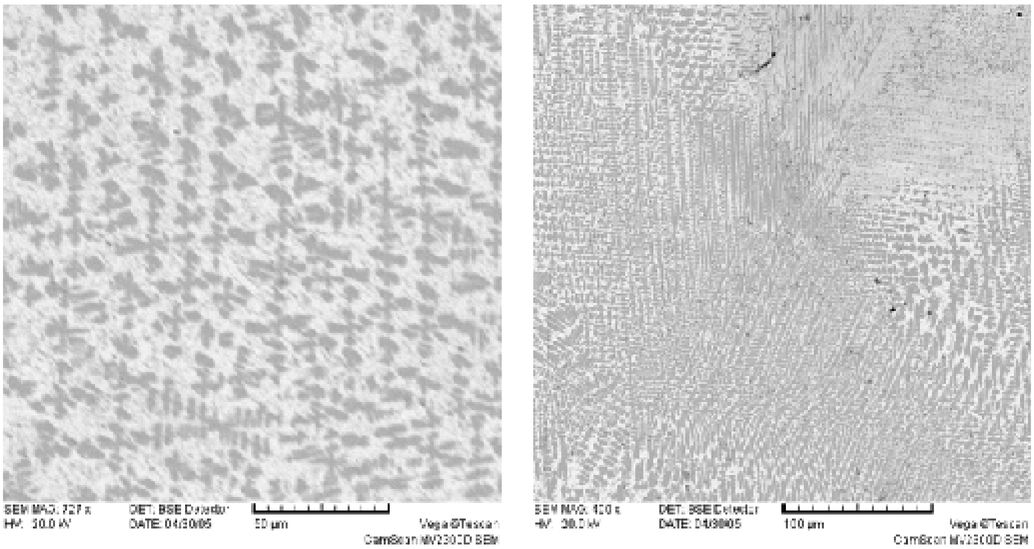

1 (SQ1) 2 (SQ2)

Fig. 3.12. Micrographs of specimens selected from sample No.3, CORD 36

Table 3.10. EDX data for specimens selected from sample No.3

No.		**U**	**Zr**	**Fe**	**O**
SQ1 top	mass%	80.36	0.84	17.12	1.68
	mol.%	44.52	1.21	40.42	13.85
	mol.%	51.67	1.41	46.92	
SQ2 bottom	mass%	77.24	0.99	19.14	2.63
	mol.%	38.52	1.29	40.68	19.51
	mol.%	47.86	1.6	50.54	

All the SEM/EDX results evidence of different character of crystallization of phases in the selected specimens and of their different ratio (Tabs. 3.8-3.10).

Fig. 3.13 shows the analyzed regions of the ingot thin section. One can see a clear boundary that conventionally separates the ingot into two parts, the top and a smaller bottom one.

Fig. 3.13. Axial section of the ingot from CORD36 (T_{liq}=2492°C) with regions marked for SEM/EDX analysis

The bottom part of the ingot was rich in rounded inclusions of UO_{2-x} (Fig. 3.14, Tab. 3.11, points P2, P6) seen against the background of the metallic matrix. Their rounded shape indicates crystallization with subsequent interaction with liquid melt. Thus, it may be supposed that at the moment of HF heating termination, this layer was liquid-solid. The metallic matrix is apparently composed of UFe_2 and U_6Fe intermetallides (Fig. 3.14, Tab. 3.11, points P3 and P1), as well as of a thin structure that reminds the eutectics (Fig. 3.14, region 1-4-2 (SQ6)).

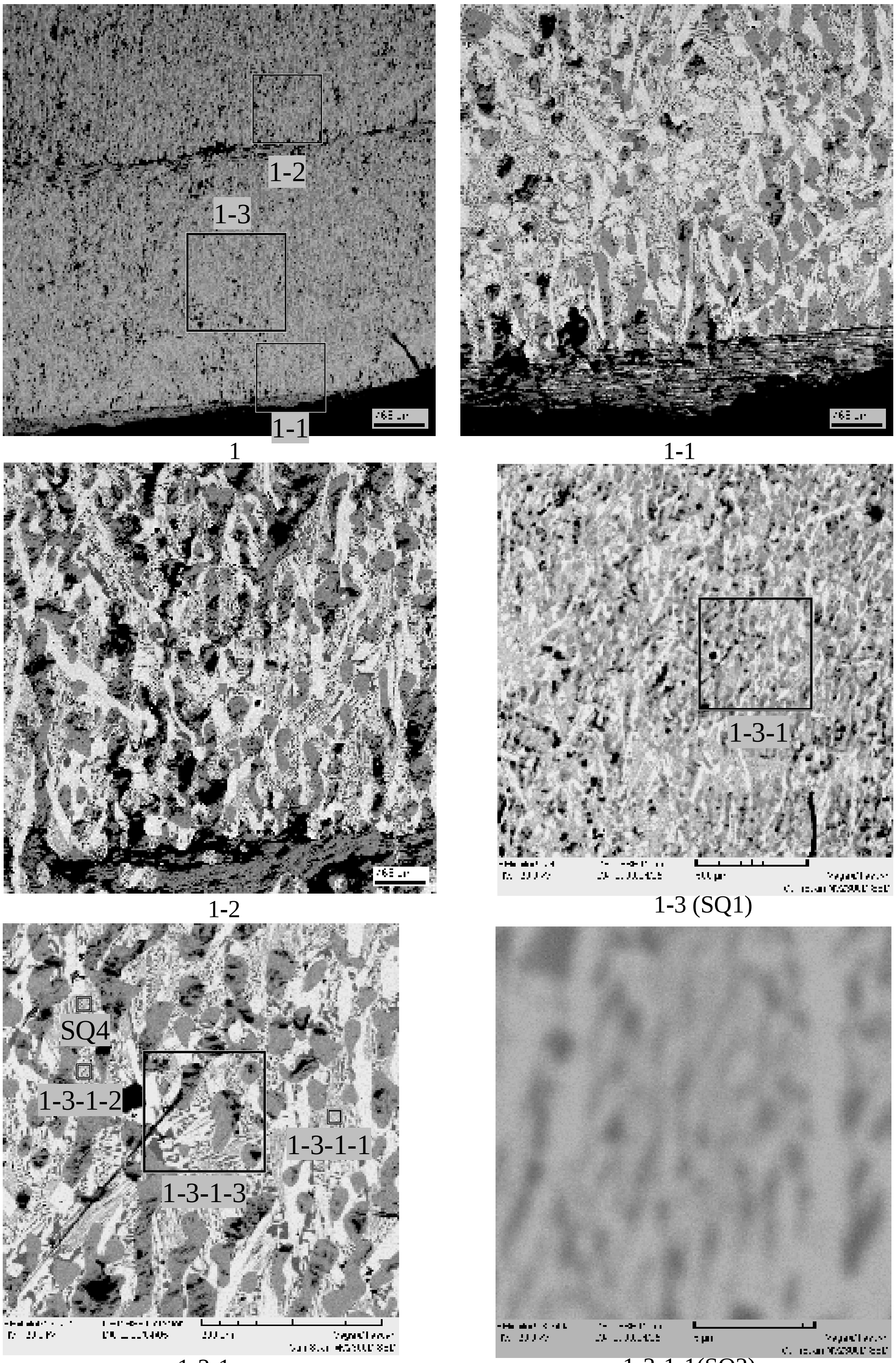

1 1-1

1-2 1-3 (SQ1)

1-3-1 1-3-1-1(SQ2)

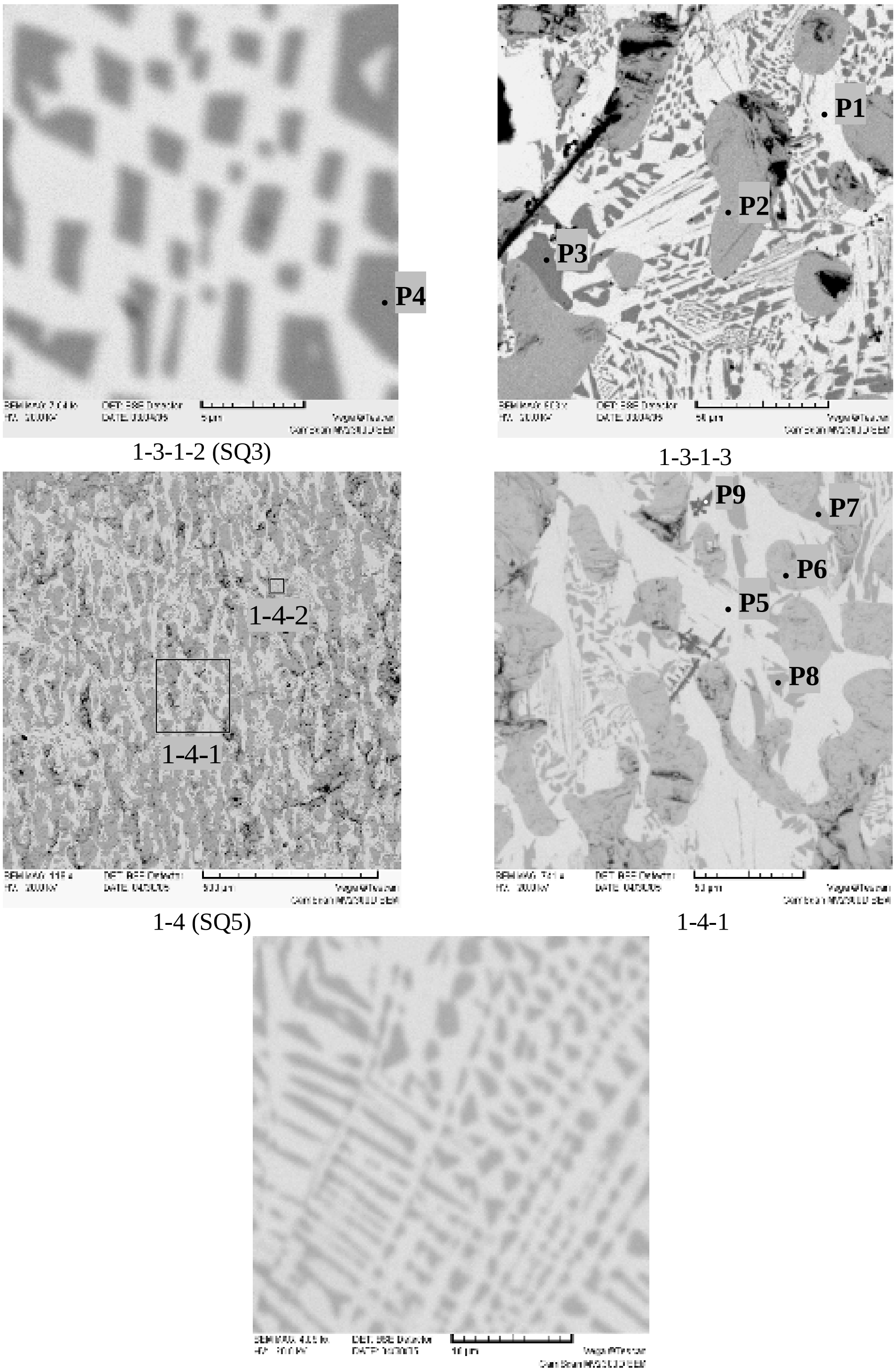

1-3-1-2 (SQ3)

1-3-1-3

1-4 (SQ5)

1-4-1

1-4-2 (SQ6)

Fig. 3.14. Micrographs of region 1 in the ingot bottom part, CORD 36

Table 3.11. EDX data for region 1 of the ingot

No.		**U**	**Zr**	**Fe**	**O**
SQ1*	mass%	88.34	-	7.57	4.09
	mol.%	48.68	-	17.78	33.53
	mol.%	73.25	-	26.75	
SQ2*	mass%	87.92	-	10.96	1.12

No.		U	Zr	Fe	O
	mol.%	58.11	-	30.88	11.01
	mol.%	65.30	-	34.70	
SQ3*	mass%	84.37	-	14.07	1.56
	mol.%	50.36	-	35.79	13.85
	mol.%	58.45	-	41.55	
SQ4*	mass%	84.07	-	14.56	1.37
	mol.%	50.49	-	37.27	12.24
	mol.%	57.53	-	42.47	
SQ5	mass%	88.45	0.8	6.23	4.52
	mol.%	47.98	1.13	14.4	36.48
	mol.%	75.54	1.78	22.68	
SQ6	mass%	83.5	1.35	13.71	1.44
	mol.%	50.04	2.11	35.02	12.84
	mol.%	57.41	2.42	40.17	
P1*	mass%	95.07	-	3.78	1.15
	mol.%	74.11	-	12.56	13.34
	mol.%	85.51	-	14.49	
P2*	mass%	92.24	-	-	7.76
	mol.%	44.41	-	-	55.59
	mol.%	100	-	-	
P3	mass%	64.07	2.59	32.28	1.06
	mol.%	28.58	3.01	61.37	7.03
	mol.%	30.74	3.24	66.02	
P4	mass%	64.21	2.31	32.08	1.40
	mol.%	28.19	2.65	60.02	9.14
	mol.%	31.02	2.91	66.06	
P5	mass%	83.5	1.35	13.71	1.44
	mol.%	50.04	2.11	35.02	12.84
	mol.%	57.41	2.42	40.17	
P6	mass%	92.15	0.64	-	7.21
	mol.%	45.83	0.83	-	53.34
	mol.%	98.22	1.78	-	
P7	mass%	60.78	3.14	34.71	1.37
	mol.%	25.61	3.45	62.34	8.59
	mol.%	28.02	3.78	68.2	
P8	mass%	61.35	2.62	34.59	1.44
	mol.%	25.88	2.88	62.2	9.04
	mol.%	28.45	3.17	68.38	
P9	mass%	9.62	89.26	-	1.12
	mol.%	3.71	89.86	-	6.43
	mol.%	3.97	96.03	-	

*) Zr excluded from calculation.

It should be noted that zirconium crystallized in the ingot bottom part both as individual inclusions (Fig. 3.14 and Tab. 3.11, point P9) and as part of UFe_2 and U_6Fe intermetallides in the form of a solid solution.

Microstructurally, the ingot top part is apparently composed of UFe_2 and U_6Fe intermetallides (Fig. 3.14 and Tab. 3.11, points P4 and P1) in the form of well-shaped grains with eutectics in between (Fig. 3.14 and Tab. 3.11, region 2-2-1-1(SQ2)).

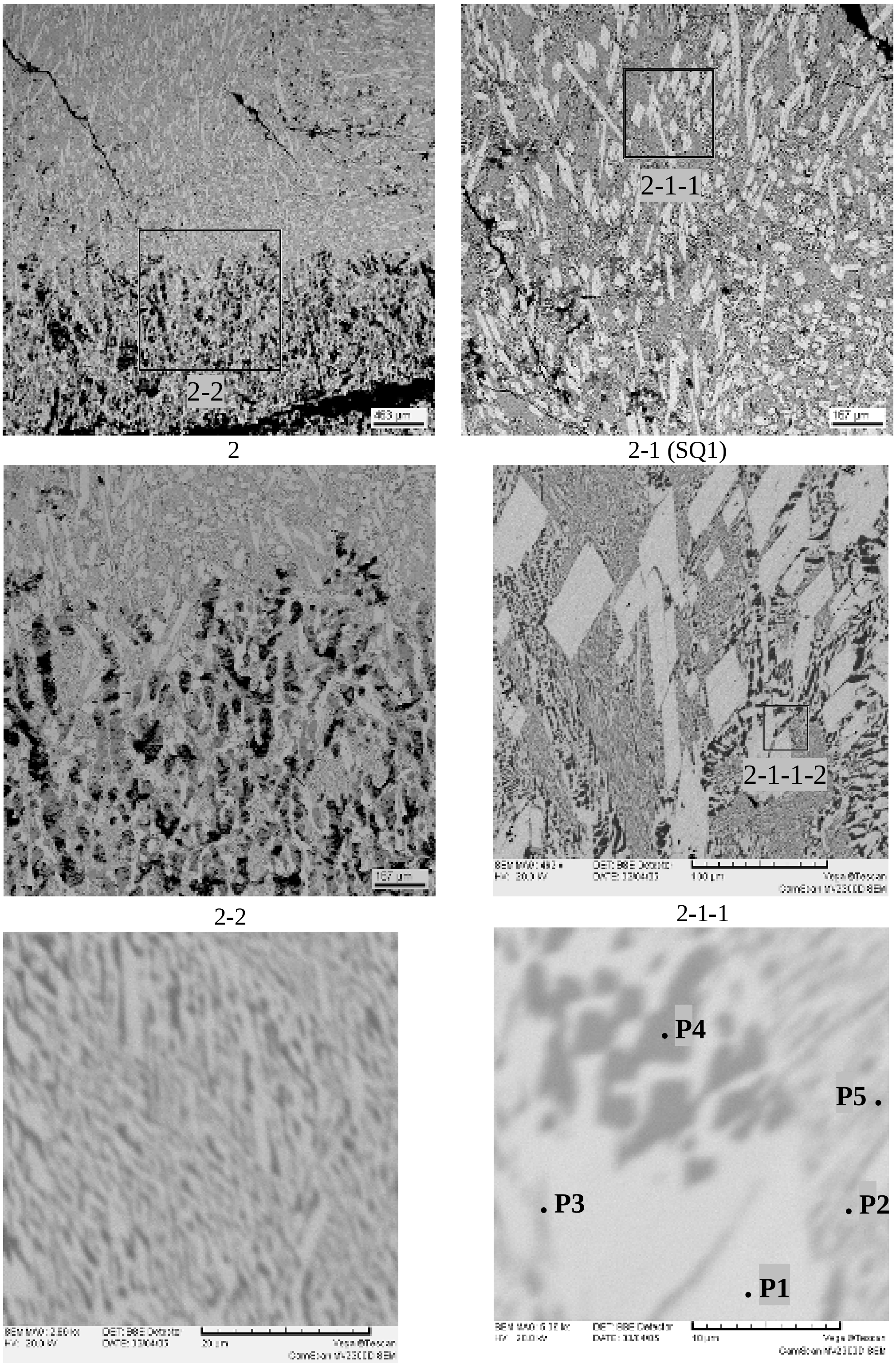

2 2-1 (SQ1)

2-2 2-1-1

2-2-1-1(SQ2) 2-1-1-2

Fig. 3.15. Micrograph of region 2 in the ingot top part, CORD 36

Table 3.12. EDX data for region 2

No.		U	Zr	Fe	O
SQ1	mass%	87.36	0.67	10.39	1.58
	mol.%	55.68	1.11	28.23	14.98
	mol.% MeO_x	65.49	1.31	33.20	
SQ2	mass%	86.05	1.04	11.59	1.32
	mol.%	54.53	1.72	31.31	12.44
	mol.% MeO_x	62.28	1.96	35.75	
P1	mass%	94.66	-	3.87	1.47
	mol.%	71.16	-	12.40	16.44
	mol.% MeO_x	85.16	-	14.84	
P2	mass%	81.68	-	17.02	1.30
	mol.%	47.06	-	41.80	11.14
	mol.% MeO_x	52.96	-	47.04	
P3	mass%	88.89	3.05	6.67	1.39
	mol.%	60.90	5.45	19.48	14.17
	mol.% MeO_x	70.95	6.35	22.69	
P4	mass%	62.99	3.12	32.59	1.30
	mol.%	27.46	3.55	60.56	8.43
	mol.% MeO_x	29.99	3.88	66.13	
P5	mass%	85.07	1.44	12.10	1.39
	mol.%	52.81	2.33	32.02	12.84
	mol.% MeO_x	60.59	2.68	36.73	

Region 3 of the ingot (Fig. 3.16) was located approximately in the middle of the top part.

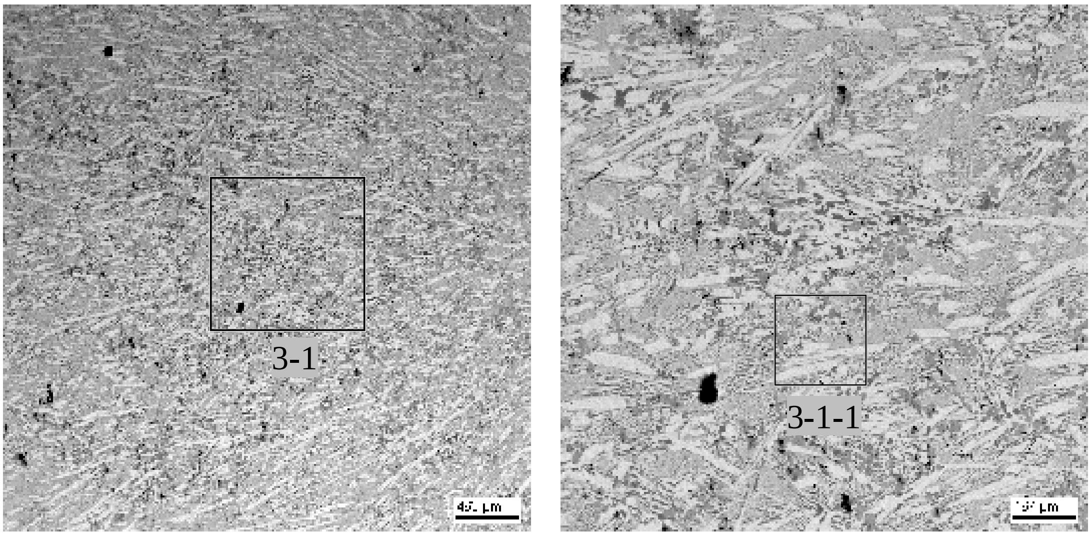

3 (SQ1) 3-1(SQ2)

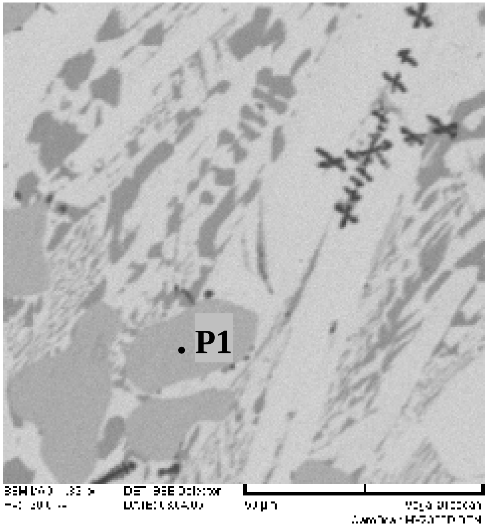

3-1-1

Fig. 3.16. Micrograph of region 3 in the ingot top part, CORD 36

Table 3.13. EDX data for region 3

No.		U	Zr	Fe	O
SQ1	mass%	88.17	-	10.26	1.57
	mol.%	56.79	-	28.17	15.04
	mol.%	66.85	-	33.15	
SQ2	mass%	86.71	1.00	10.37	1.92
	mol.%	53.50	1.61	27.27	17.62
	mol.%	64.94	1.95	33.10	
P1	mass%	91.60	0.63	-	7.77
	mol.%	43.86	0.79	-	55.35
	mol.%	98.24	1.76	-	

Region 3, like the bottom part of the ingot, was found to contain rounded inclusions of UO_{2-x} (Fig. 3.16 and Tab. 3.13, point P1).

Region 4 of the ingot upper part is obviously also a mixture of UFe_2 and U_6Fe intermetallides (Fig. 3.17 and Tab. 3.14, points P2 and P1) in the form of well-shaped grains with eutectics in between (Fig. 3.17, fragments of region 4-1).

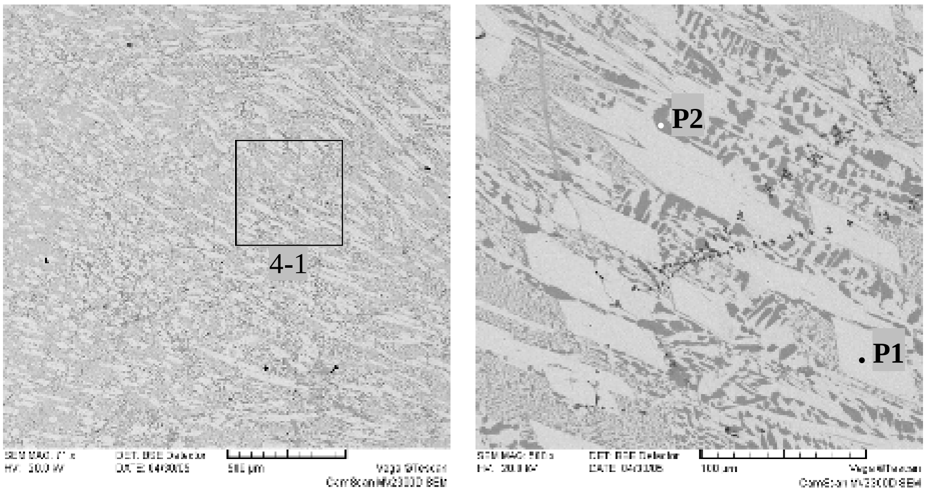

4 (SQ1) 4-1

Fig. 3.17. Micrographs of region 4 in the ingot top part, CORD 36

Table 3.14. EDX data for region 4

No.		U	Zr	Fe	O
SQ1	mass%	85.64	1.26	11.45	1.65
	mol.%	52.77	2.03	30.07	15.13
	mol.%	62.18	2.39	35.43	
P1	mass%	94.5	-	3.89	1.61
	mol.%	69.98	-	12.28	17.74
	mol.%	85.07	-	14.93	
P2	mass%	61.99	2.42	34.26	1.33
	mol.%	26.48	2.7	62.37	8.45
	mol.%	28.93	2.95	68.13	

Region 5 in the ingot top part was similar to the ones described above with one exception that U_6Fe intermetallide segregated here as light-coloured extended strips (Fig. 3.18).

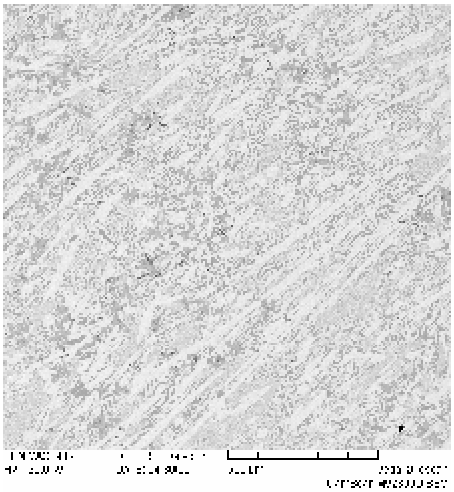

5 (SQ1)

Fig. 3.18. Micrograph of region 5 in the ingot top part, CORD 36

Table 3.17. EDX data for region 5

No.		U	Zr	Fe	O
SQ1	mass%	85.14	1.14	11.49	2.23
	mol.%	50	1.75	28.76	19.49
	mol.%	62.11	2.17	35.72	

CORD40

Fig. 3.19 shows the axial section of the ingot with regions marked for investigation. Here one can also clearly see two layers, the upper and lower ones, but in contrast to the previous test (Fig. 3.13) the lower layer is more metal-rich and occupies a much bigger volume.

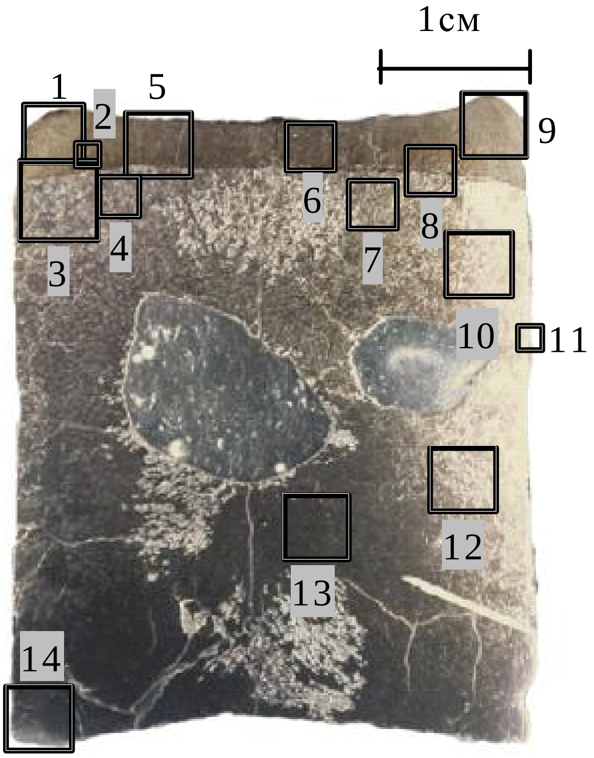

Fig. 3.19. Axial section of the ingot from CORD40 (T_{liq}=2515°C) with regions marked for SEM/EDX analysis

The results of SEM/EDX analysis for the studied regions are given in Figs. 3.19-3.31 and in Tabs. 3.16-3.26.

The ingot top part was found to have a layer containing much oxygen (oxide-rich). Microstructure of its separate regions is presented in Figs. 3.20, 3.21, 3.24, 3.25 and 3.28.

Microstructure of this layer upper part is highly porous (Fig. 3.20, regions 1-1 and 1-2) and is practically identical to a structure that can be observed after the monotectic decomposition of a light refractory liquid in the U-O system /6 /. The main phases of this layer are UO_{2-x} and U (Fig. 3.20 and Tab. 3.16, SQ3, SQ4, points P1 and P3, respectively). Iron is virtually absent in this layer (Fig. 3.20, region 1-1-1 and Tab. 3.16, region SQ2). At the same time, the boundary area features metal-rich globules that accumulate about 2 mol. % Fe (Fig. 3.24, region 5-1-2 and Tab. 3.20, SQ3). The presence of Zr in the sample is explained by its presence in the initial U reagent and $UO_{2.24}$ (see Tab. 3.1)

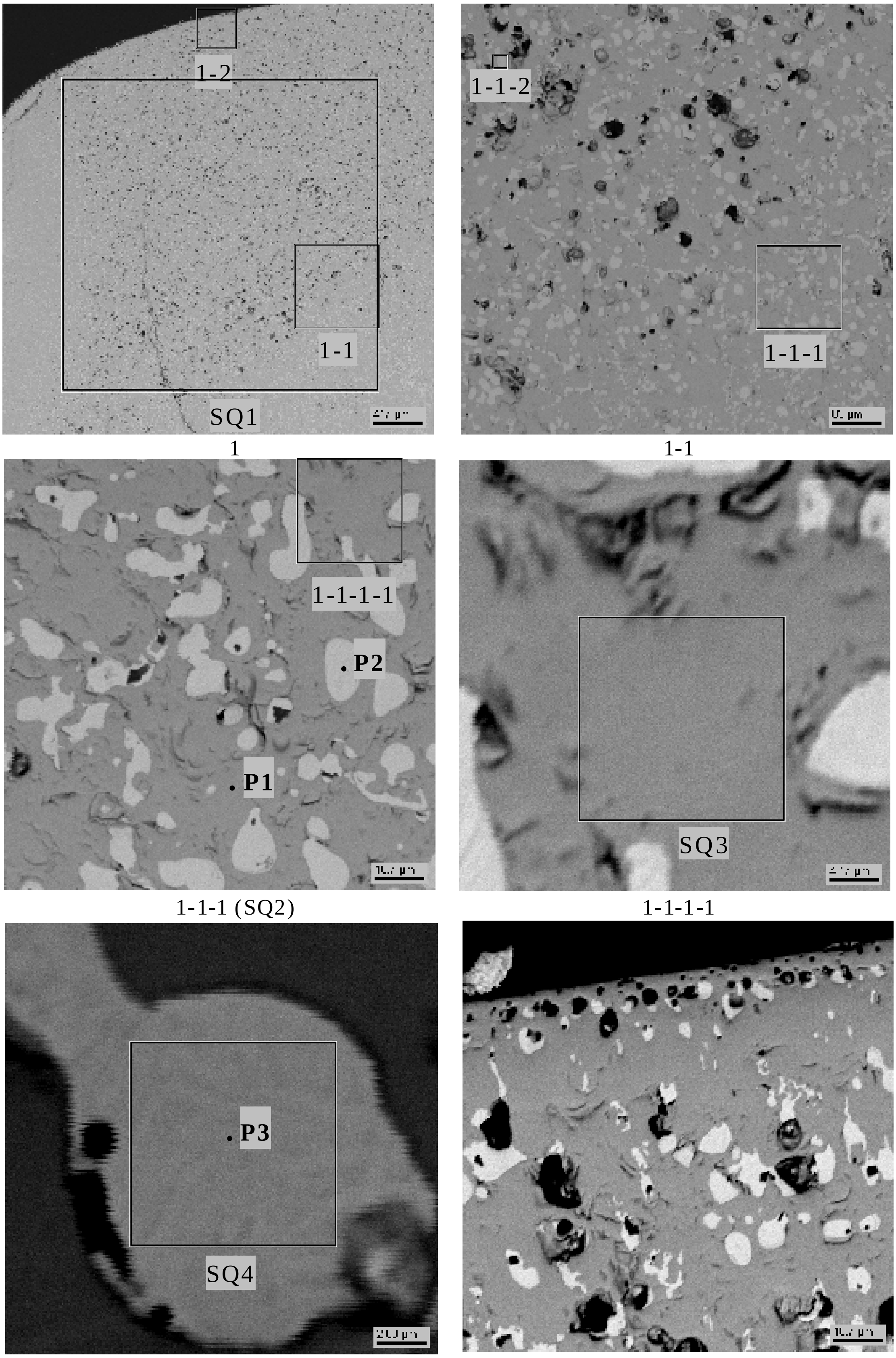

1 1-1

1-1-1 (SQ2) 1-1-1-1

1-1-2 1-2

Fig. 3.20. Micrographs of region 1 in the upper part of the ingot top layer, CORD 40; black rounded formations are pores

Table 3.16. EDX data for regions 1

No.		U	Zr	Fe	~O
SQ1	mass%	84.17	1.61	0.34	13.89
	mol.%	28.40	1.42	0.48	69.70
	mol.% MeO_x	93.72	4.68	1.60	
SQ2	mass%	85.58	1.54	-	12.88
	mol.%	30.44	1.43	-	68.14
	mol.% MeO_x	95.52	4.48	-	
SQ3	mass%	87.43	1.00	-	11.57
	mol.%	33.34	0.99	-	65.66
	mol.% MeO_x	97.11	2.89	-	
SQ4	mass%	91.61	2.23	-	6.16
	mol.%	48.46	3.07	-	48.47
	mol.% MeO_x	94.04	5.96	-	
P1	mass%	87.30	0.67	-	12.04
	mol.%	32.56	0.65	-	66.79
	mol.% MeO_x	98.05	1.95	-	
P2	mass%	92.81	0.84	-	6.35
	mol.%	48.97	1.16	-	49.87
	mol.% MeO_x	97.69	2.31	-	
P3	mass%	98.68	0.75	0.57	-
	mol.%	95.75	1.90	2.34	-

The lower part of the oxide-rich top layer is less porous and includes globules of the second liquid (Fig. 3.21, regions 2 and 2-1; 3.22, regions 5-1-1 и 5-1-2) that apparently contains U_6Fe (Tab. 3.17, SQ3, points P2 and P3), a small quantity of UFe_2 (Tab. 3.17, points P9 and P10) and the phase of a ternary intermetallic compound (Tab. 3.17, point P6). Formation of the latter was determined by presence of Zr in the sample. Such globules may be either a result of the secondary separation from the oxidic liquid at reaching the monotectic temperature by the melt (when the melt cools down), or a consequence of the temperature gradient under the experimental conditions /18/.

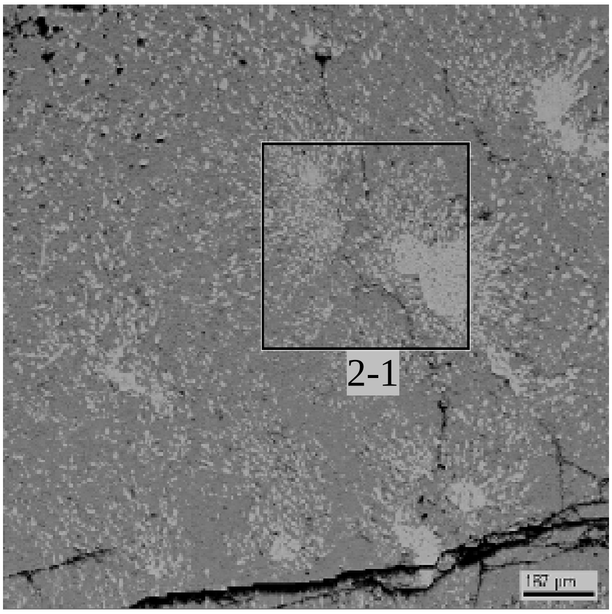

2 (SQ1)

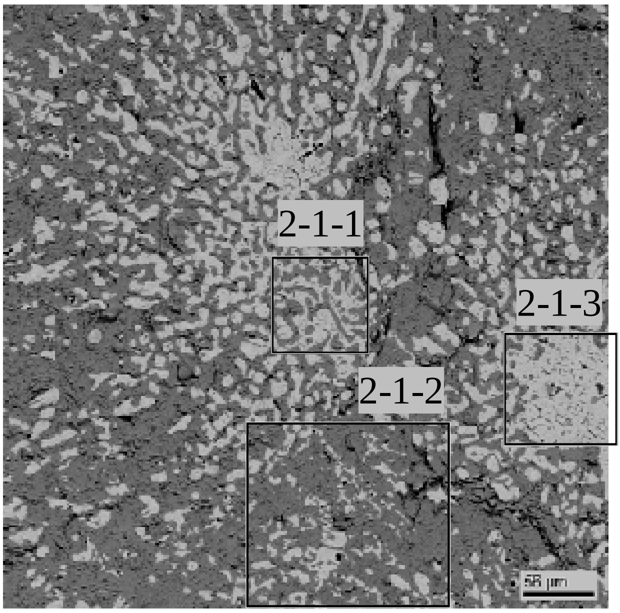

2-1

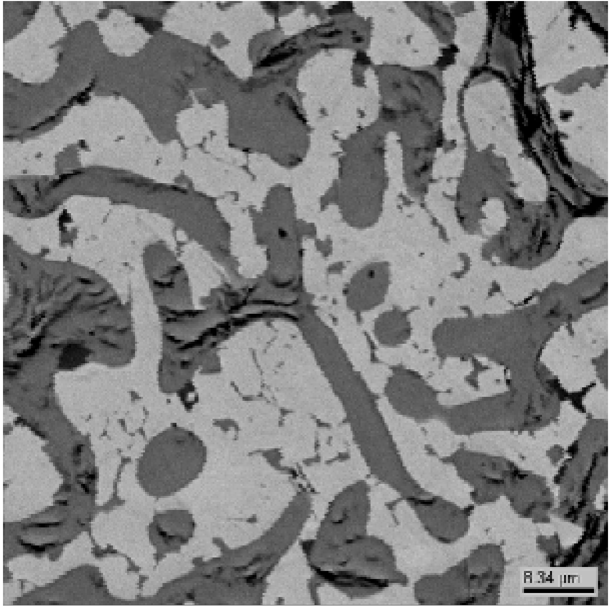

2-1-1

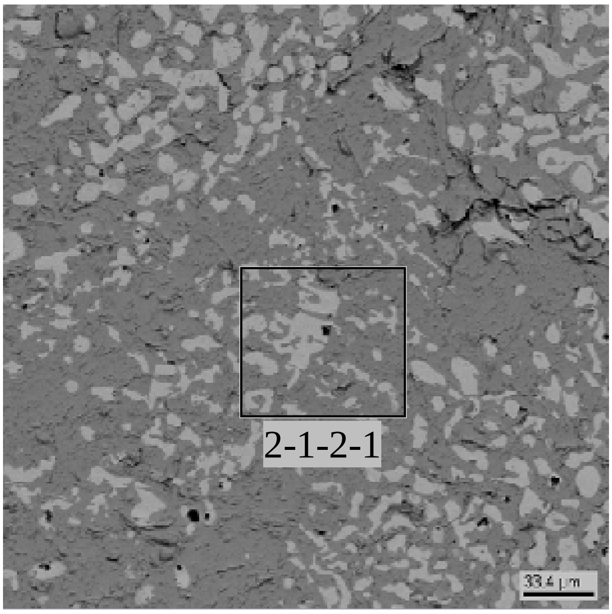

2-1-2 (SQ2)

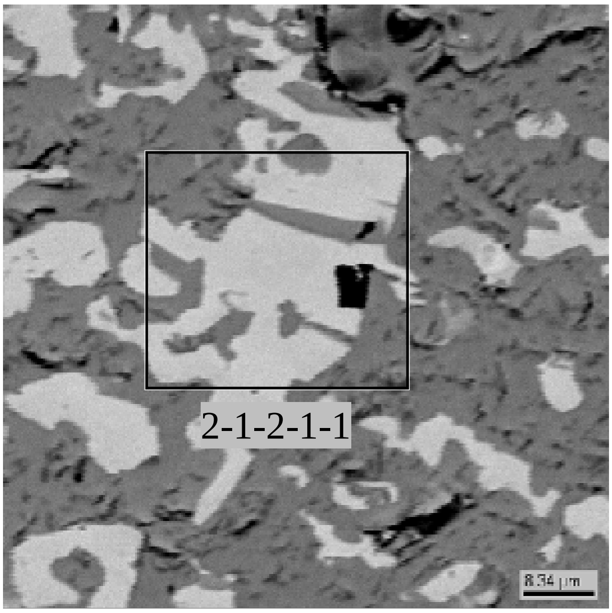

2-1-2-1

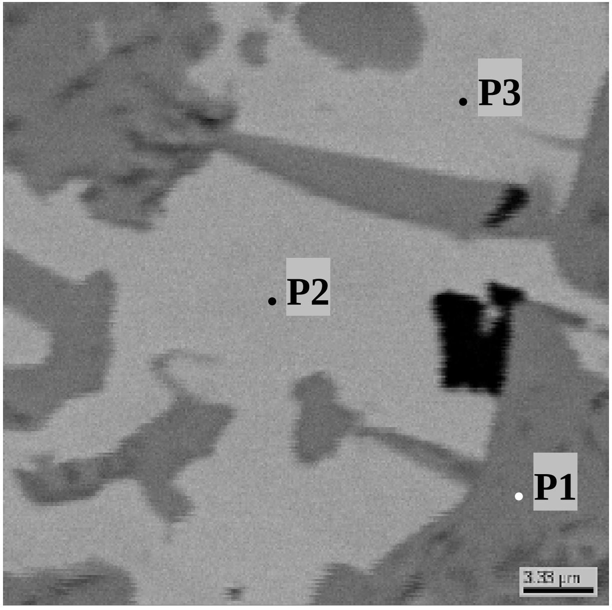

2-1-2-1-1

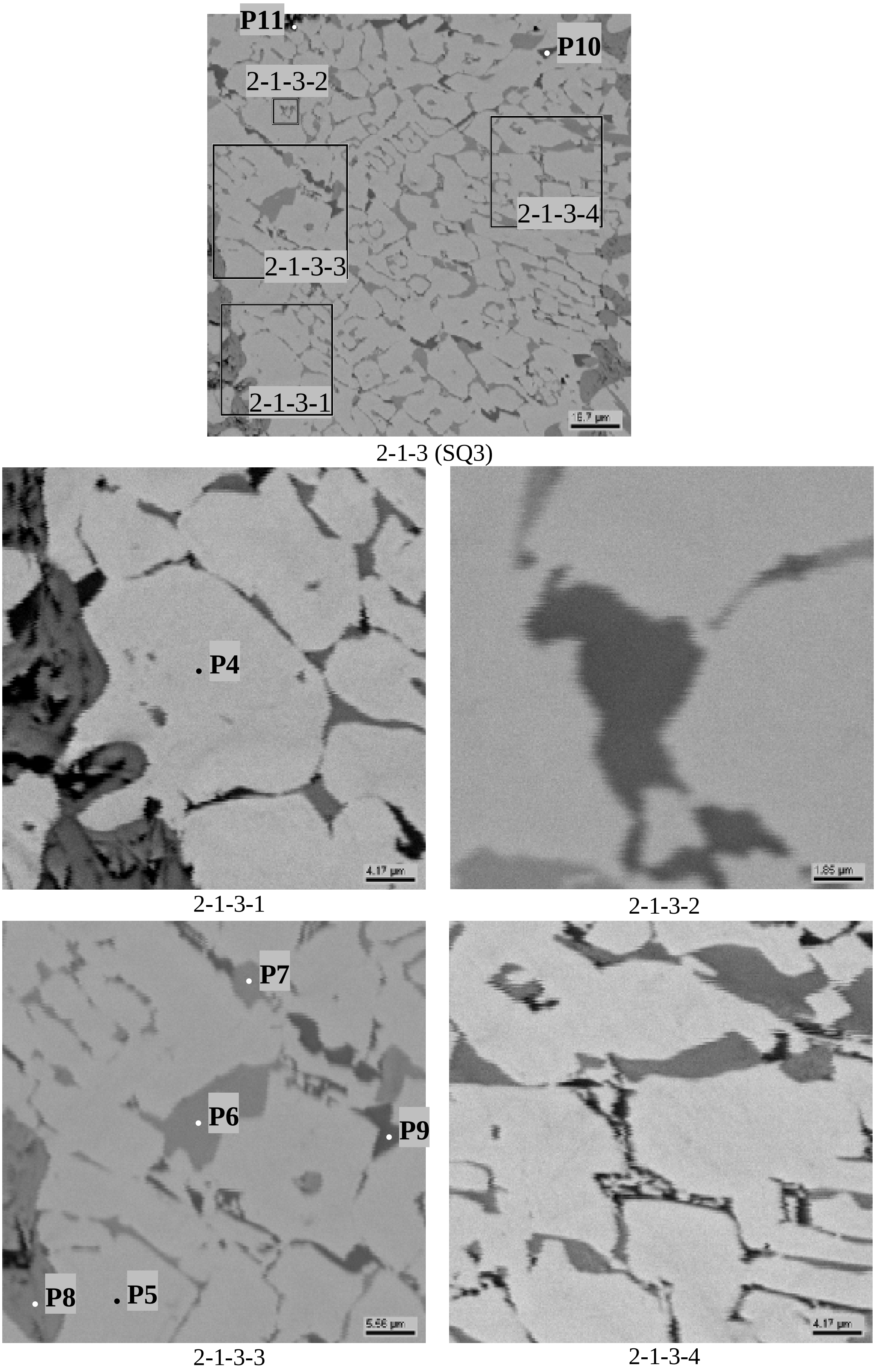

2-1-3 (SQ3)

2-1-3-1

2-1-3-2

2-1-3-3

2-1-3-4

Fig. 3.21. Micrograph of region 2 in the lower part of the ingot top layer, CORD 40

Table 3.17. EDX data for region 2

No.		U	Zr	Fe	~O
SQ1	mass%	84.28	1.19	1.51	13.02
	mol.%	29.31	1.08	2.23	67.38
	mol.% MeO_x	89.86	3.30	6.84	
SQ2	mass%	88.01	1.10	2.07	8.82
	mol.%	38.12	1.24	3.82	56.82
	mol.% MeO_x	88.28	2.87	8.85	
SQ3	mass%	92.44	1.14	6.42	-
	mol.%	75.29	2.42	22.29	-
P1	mass%	86.90	1.18	-	11.93
	mol.%	32.49	1.15	-	66.36
	mol.% MeO_x	96.59	3.41	-	
P2	mass%	95.45	0.50	4.05	-
	mol.%	83.71	1.14	15.15	-
P3	mass%	95.34	0.48	4.19	-
	mol.%	83.32	1.09	15.59	-
P4	mass%	95.90	-	4.10	-
	mol.%	84.59	-	15.41	-
P5	mass%	95.43	0.32	4.25	-
	mol.%	83.43	0.72	15.85	-
P6	mass%	75.05	7.76	14.41	2.79
	mol.%	37.87	10.21	30.99	20.93
	mol.% MeO_x	47.89	12.92	39.19	
P7	mass%	74.89	7.62	14.45	3.04
	mol.%	37.16	9.86	30.56	22.42
	mol.% MeO_x	47.90	12.71	39.39	
P8	mass%	87.01	0.75	-	12.24
	mol.%	32.09	0.72	-	67.19
	mol.% MeO_x	97.81	2.19	-	
P9	mass%	57.20	6.13	36.66	-
	mol.%	24.93	6.97	68.10	-
P10	mass%	55.70	7.05	37.25	-
	mol.%	23.92	7.90	68.18	-
P11	mass%	33.27	52.27	3.21	11.25
	mol.%	9.49	38.89	3.91	47.72
	mol.% MeO_x	18.14	74.39	7.47	

Fig. 3.22 presents the upper peripheral part of the ingot bottom layer and the boundary region. Uneven distribution of phases is visible here. The bottom layer of the boundary region

(3-2, 3-3) features globules that contain UO_{2-x} (Tab. 3.18, SQ3, SQ4) and, possibly, U and U_6Fe (the points were not analyzed). Thus, the composition of globules in the bottom layer of the boundary region is similar to the total composition of the oxide-rich upper layer (Tab. 3.16, SQ1 and 3.18, SQ4).

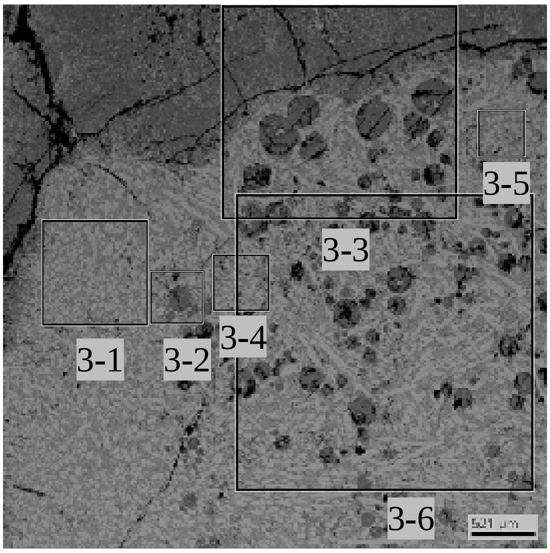

3

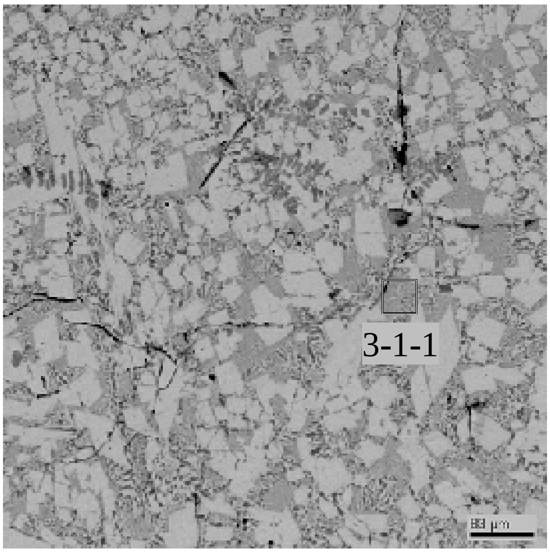

3-1 (SQ1)

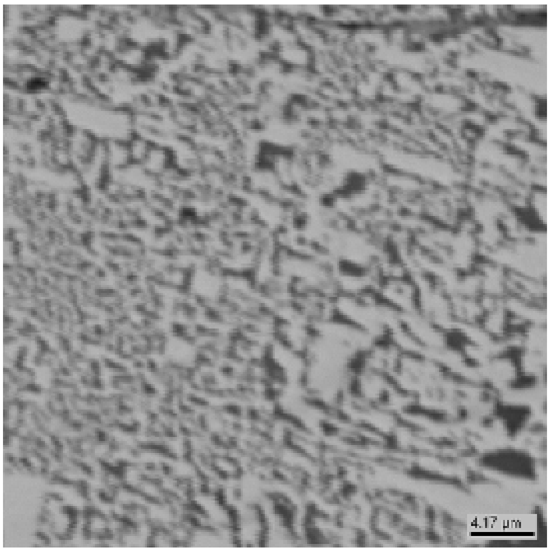

3-1-1 (SQ2)

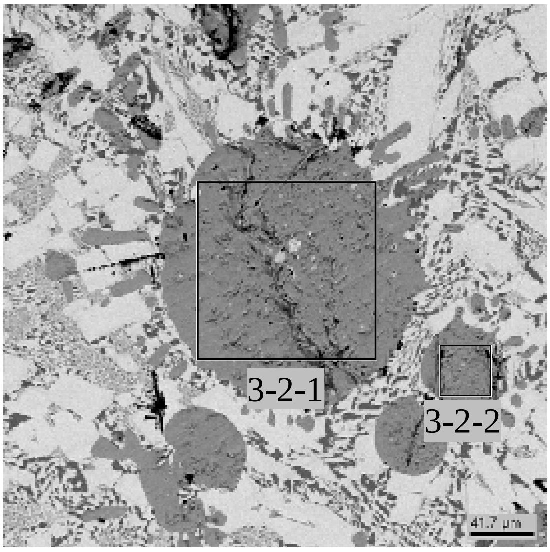

3-2

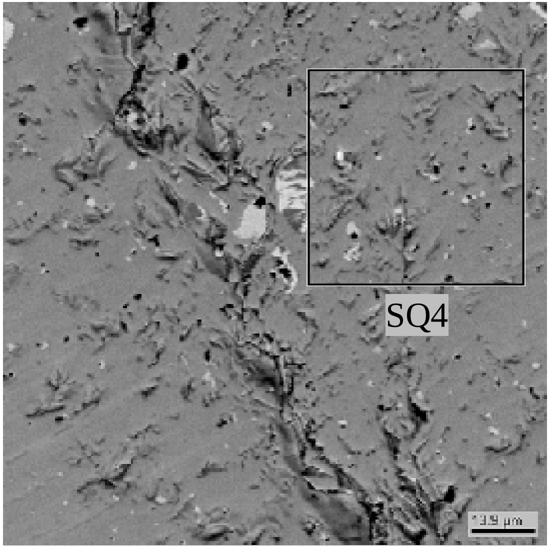

3-2-1 (SQ3)

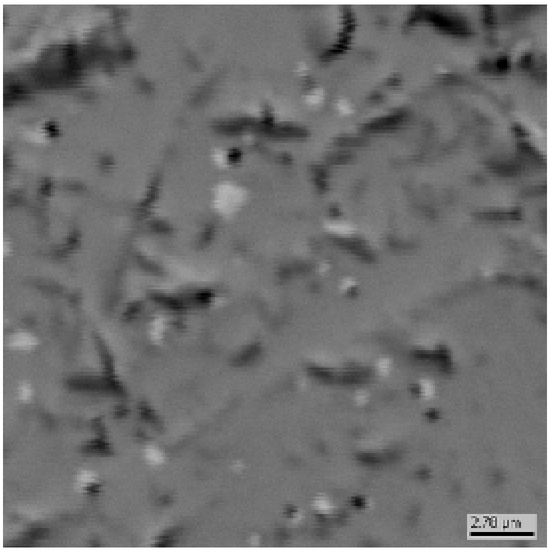

3-2-2 (SQ5)

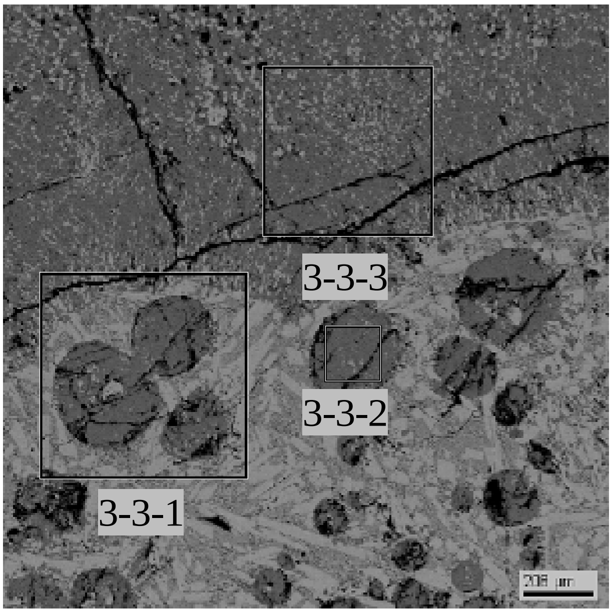

3-3

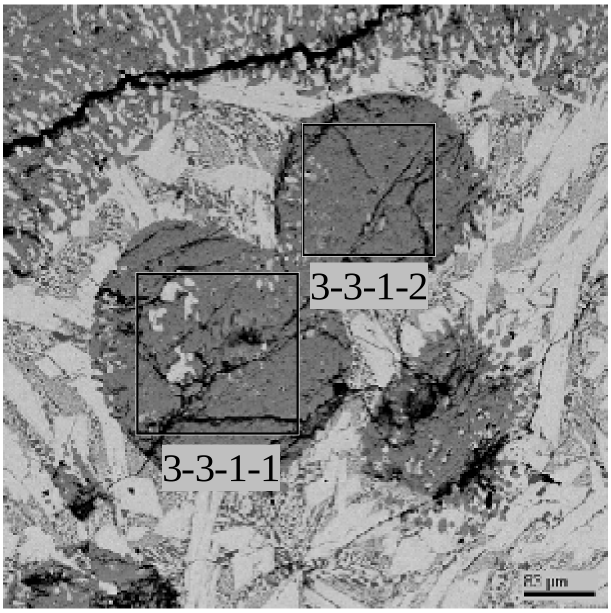

3-3-1

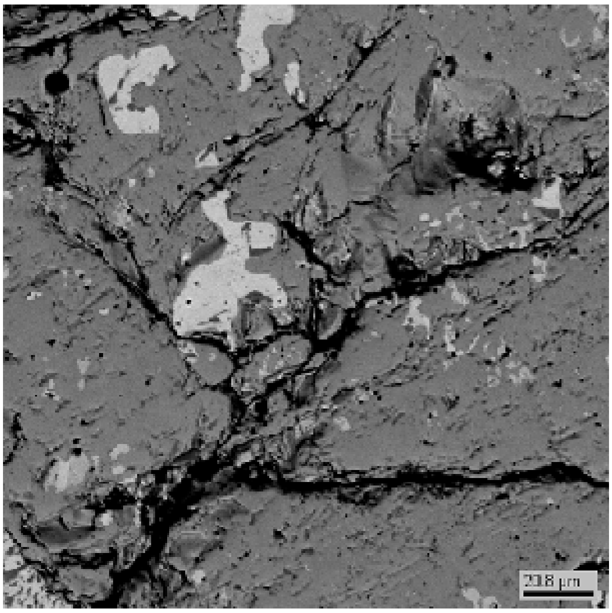

3-3-1-1 (SQ6)

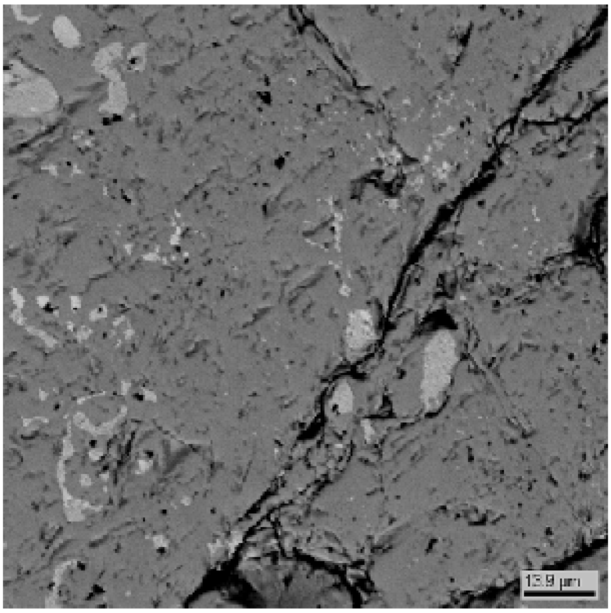

3-3-1-2 (SQ7)

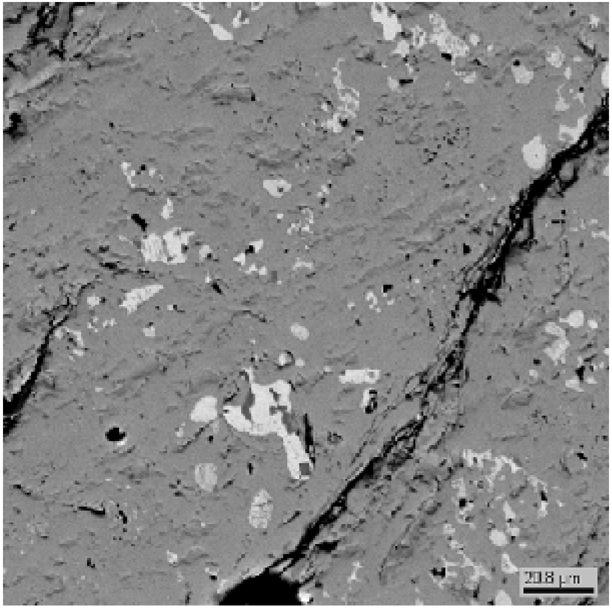

3-3-2 (SQ8)

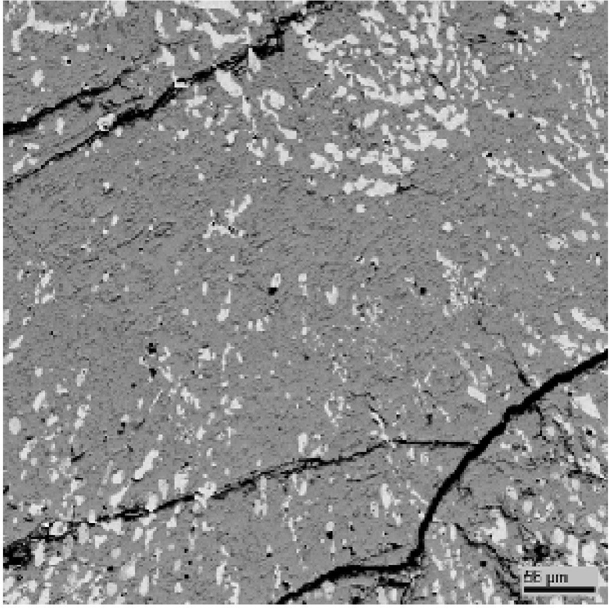

3-3-3 (SQ9)

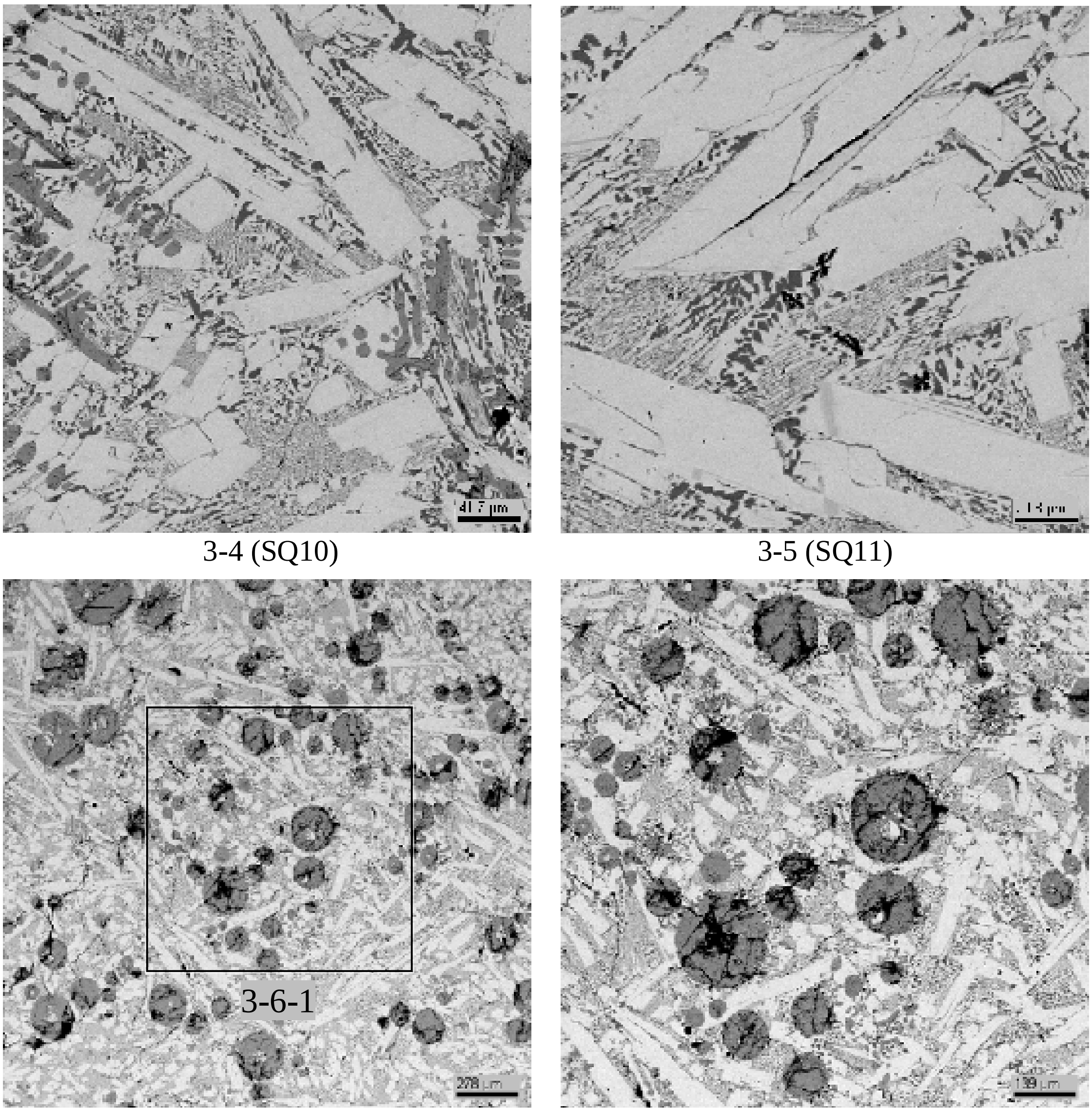

3-4 (SQ10) 3-5 (SQ11)

3-6 (SQ12) 3-6-1 (SQ13)

Fig. 3.22. Micrograph of region 3 in the bottom layer and boundary region of the ingot, CORD 40

Table 3.18. EDX data for region 3

No.		**U**	**Zr**	**Fe**	**~O**
SQ1	mass%	89.36	0.74	9.90	-
	mol.%	66.95	1.45	31.60	-
SQ2	mass%	86.12	1.17	12.72	-
	mol.%	60.07	2.12	37.80	-
SQ3	mass%	87.56	1.42	1.26	9.76
	mol.%	36.21	1.53	2.21	60.05
	mol.% MeO_x	90.62	3.84	5.54	
SQ4	mass%	86.90	1.44	0.66	10.99
	mol.%	33.81	1.47	1.10	63.62
	mol.% MeO_x	92.95	4.03	3.02	
SQ5	mass%	87.38	1.43	0.33	10.87
	mol.%	34.38	1.46	0.55	63.61

No.		U	Zr	Fe	~O
	mol.% MeO_x	94.46	4.02	1.52	
SQ6	mass%	83.94	1.08	1.55	13.43
	mol.%	28.64	0.96	2.25	68.15
	mol.% MeO_x	89.91	3.03	7.07	
SQ7	mass%	85.98	1.32	0.88	11.82
	mol.%	31.96	1.28	1.39	65.37
	mol.% MeO_x	92.29	3.71	4.01	
SQ8	mass%	85.46	1.47	1.24	11.83
	mol.%	31.59	1.42	1.95	65.04
	mol.% MeO_x	90.36	4.06	5.58	
SQ9	mass%	86.45	1.23	1.67	10.64
	mol.%	33.88	1.26	2.79	62.07
	mol.% MeO_x	89.31	3.32	7.37	
SQ10	mass%	90.02	0.83	9.15	-
	mol.%	68.62	1.66	29.73	-
SQ11	mass%	89.94	0.81	9.25	-
	mol.%	68.40	1.61	29.99	-
SQ12	mass%	88.12	0.88	8.00	3.00
	mol.%	52.08	1.36	20.14	26.41
	mol.% MeO_x	70.78	1.85	27.37	
SQ13	mass%	90.21	0.94	8.04	0.81
	mol.%	64.91	1.77	24.66	8.66
	mol.% MeO_x	71.06	1.94	27.00	

Region 4, marked in the ingot (Fig. 3.19), and its microstructure (Fig. 3.23) show a picture that is similar to the previous one. Like in region 3, here one can see globules that are characteristic of the top layer of the lower liquid (Fig. 3.22, region 3-3-1 or 3-6-1).

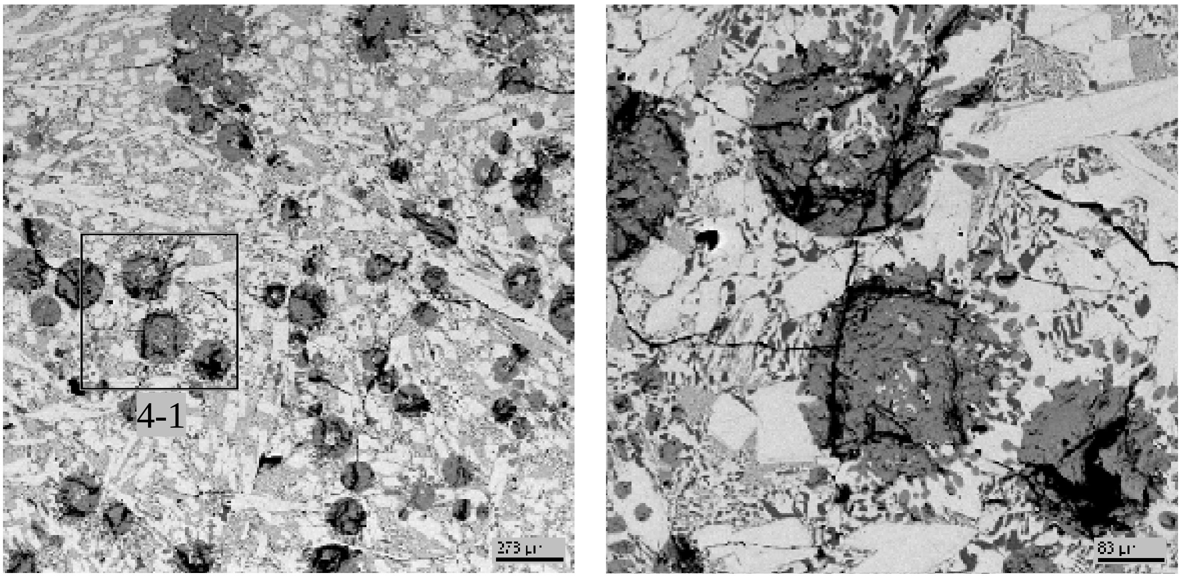

4 (SQ1) 4-1

Fig. 3.23. Micrograph of region 4 in the top part of the ingot bottom layer, CORD 40

Table 3.19. EDX data for region 4

No.		U	Zr	Fe	~O
SQ1	mass%	87.76	0.88	8.52	2.84
	mol.%	52.03	1.37	21.52	25.09
	mol.% MeO_x	69.45	1.82	28.73	▨

Region 5 of the ingot occupies all of its top layer and the boundary region between the layers (Fig. 3.24). Well visible is the upper porous part of the layer that contains no iron (Tab. 3.20, SQ2), then goes the boundary region of the upper layer with metal-rich globules (Tab. 3.21, SQ4, SQ5) that accumulate up to 2 mol. % of iron, and the upper part of the bottom layer with the oxidized globules (Tab. 3.23, regions 5-2, 5-2-1).

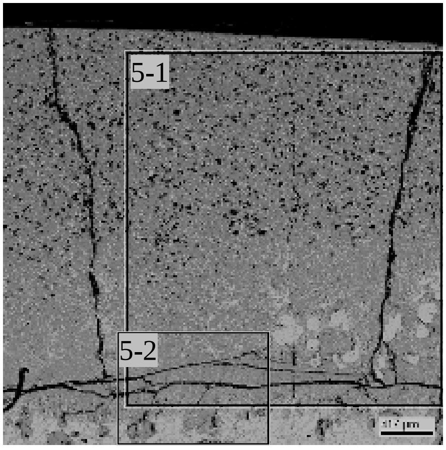

5

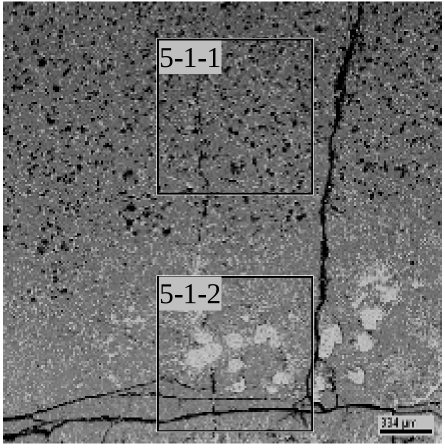

5-1 (SQ1)

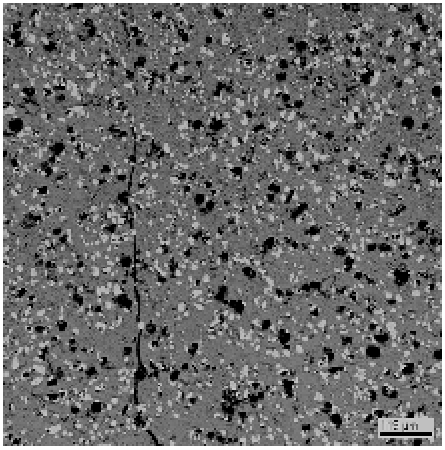

5-1-1 (SQ2)

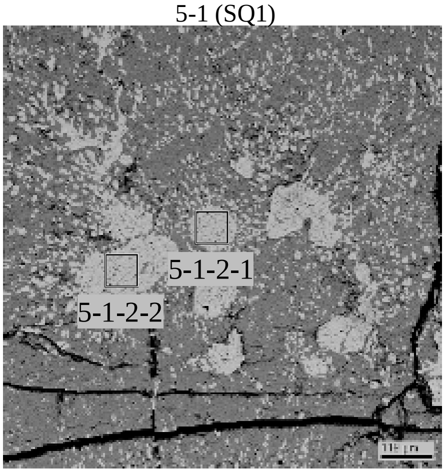

5-1-2 (SQ3)

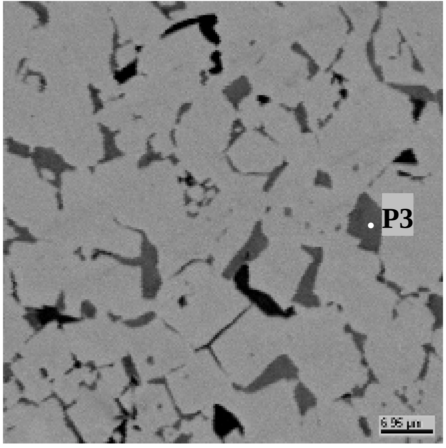

5-1-2-1 (SQ4)

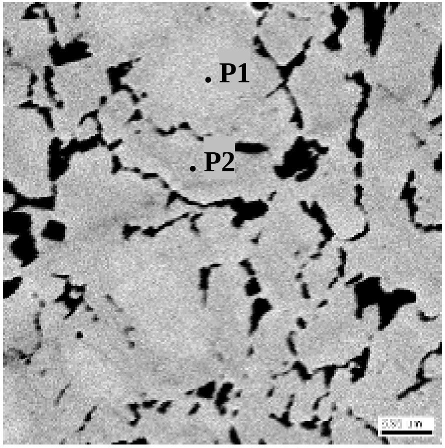

5-1-2-2 (SQ5)

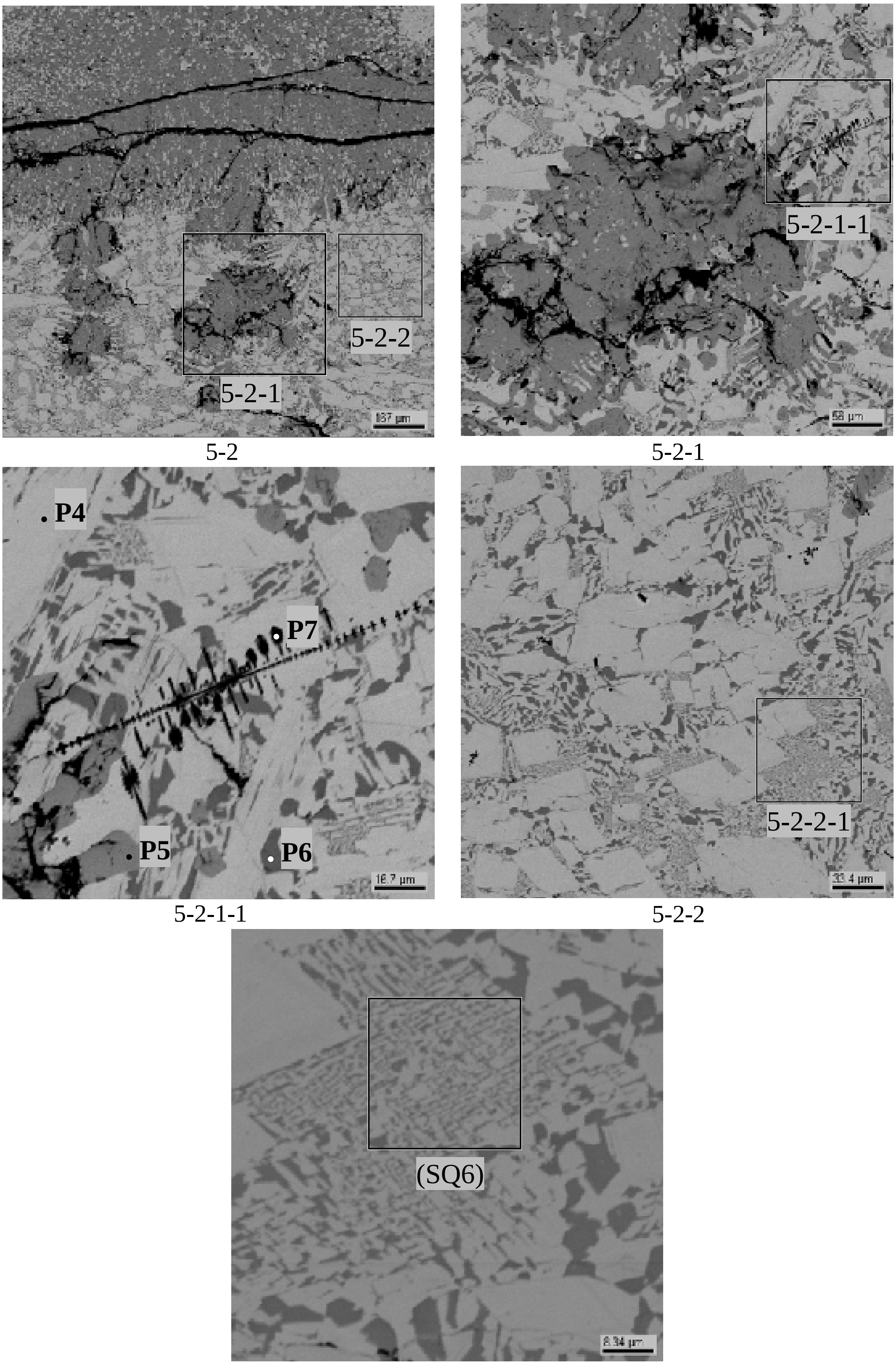

5-2 5-2-1

5-2-1-1 5-2-2

5-2-2-1

Fig. 3.24. Micrographs of region 5 in the top and a part of the bottom layers of the ingot, CORD 40

Table 3.20. EDX data for region 5

No.		U	Zr	Fe	~O
SQ1	mass%	73.69	1.20	0.96	24.14
	mol.%	16.74	0.71	0.93	81.61
	mol.% MeO$_x$	91.06	3.88	5.06	
SQ2	mass%	82.68	1.38	-	15.93
	mol.%	25.57	1.12	-	73.31
	mol.% MeO$_x$	95.82	4.18	-	
SQ3	mass%	86.17	1.23	1.48	11.13
	mol.%	32.99	1.23	2.41	63.38
	mol.% MeO$_x$	90.08	3.35	6.58	
SQ4	mass%	92.71	1.47	5.82	-
	mol.%	76.40	3.17	20.44	-
SQ5	mass%	93.41	1.75	4.84	-
	mol.%	78.76	3.86	17.39	-
SQ6	mass%	78.43	1.03	11.5	9.04
	mol.%	29.63	1.02	18.52	50.83
	mol.% MeO$_x$	60.27	2.07	37.67	
P1	mass%	99.57	0.43	-	-
	mol.%	98.89	1.11	-	-
P2	mass%	94.92	0.85	4.23	-
	mol.%	82.41	1.91	15.67	-
P3	mass%	72.99	12.16	14.85	-
	mol.%	43.44	18.89	37.67	-
P4	mass%	84.15	-	3.69	12.17
	mol.%	29.96	-	5.59	64.45
	mol.% MeO$_x$	84.27	-	15.73	
P5	mass%	84.12	0.57	-	15.31
	mol.%	26.84	0.48	-	72.68
	mol.% MeO$_x$	98.25	1.75	-	
P6	mass%	58.78	2.92	33.59	4.71
	mol.%	21.02	2.73	51.2	25.05
	mol.% MeO$_x$	28.04	3.64	68.32	
P7	mass%	29.38	47.79	1.65	21.18
	mol.%	6.17	26.18	1.48	66.17
	mol.% MeO$_x$	18.23	77.4	4.37	

Region 6 of the ingot (Fig. 3.25) is similar microstructurally to region 5. Well visible is the porous top part that contains virtually no iron (Tab. 3.21, SQ1**)** and the boundary region with the metal-rich globules.

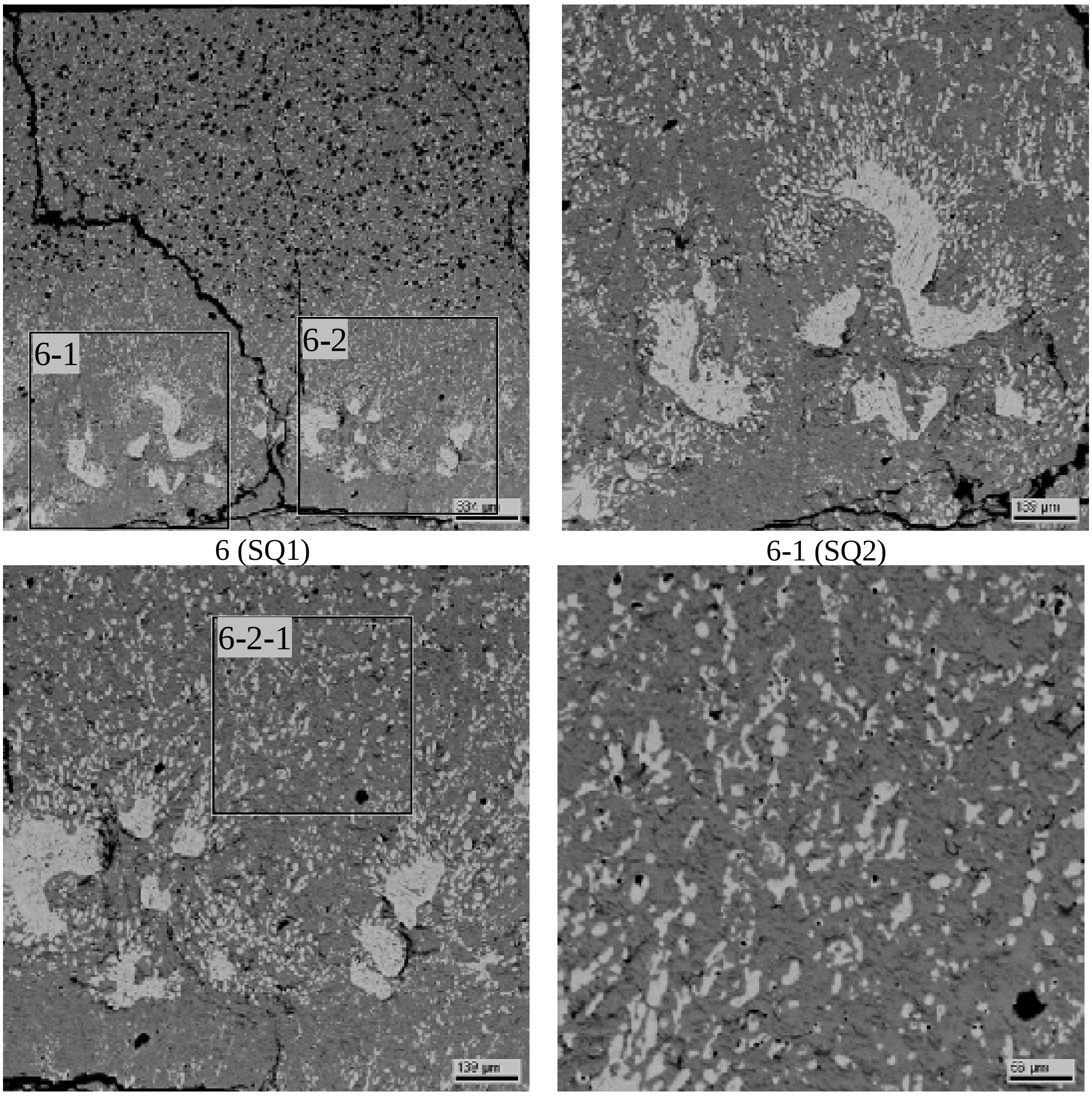

6 (SQ1) 6-1 (SQ2)

6-2 (SQ3) 6-2-1 (SQ4)

Fig. 3.25. Micrographs of region 6 in the top layer of the ingot, CORD 40

Table 3.21. EDX data for region 6

No.		U	Zr	Fe	~O
SQ1	mass%	68.78	1.13	0.95	29.14
	mol.%	13.50	0.58	0.79	85.12
	mol.% MeO$_x$	90.77	3.89	5.34	
SQ2	mass%	87.37	1.23	1.73	9.68
	mol.%	36.12	1.33	3.04	59.51
	mol.% MeO$_x$	89.21	3.29	7.51	
SQ3	mass%	85.85	1.38	1.11	11.67
	mol.%	32.07	1.34	1.76	64.83
	mol.% MeO$_x$	91.18	3.81	5.01	
SQ4	mass%	89.13	1.12	0.95	8.80
	mol.%	39.26	1.29	1.78	57.68
	mol.% MeO$_x$	92.75	3.05	4.20	

Microstructurally, region 7 (Fig. 3.26) is close to regions 3 and 4 of the ingot described above (Figs. 3.22, 3.23). This is the upper part of the ingot bottom layer with the oxide-rich globules.

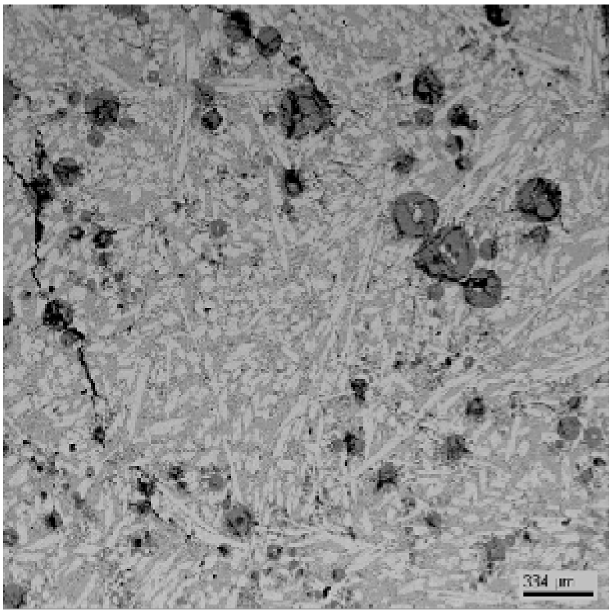

7 (SQ1)

Fig. 3.26. Micrograph of region 7 of the ingot bottom layer, CORD 40

Table 3.22. EDX data for region 7

No.		U	Zr	Fe	~O
SQ1	mass%	85.20	0.78	8.53	5.49
	mol.%	41.51	0.99	17.71	39.79
	mol.% MeO_x	68.94	1.65	29.42	

Like regions 3-5 and 7, region 8 of the ingot (Fig. 3.27) gives an idea about microstructure in the boundary region with fragments of the metal-rich globules in the upper liquid and of the oxide-rich ones in the lower liquid.

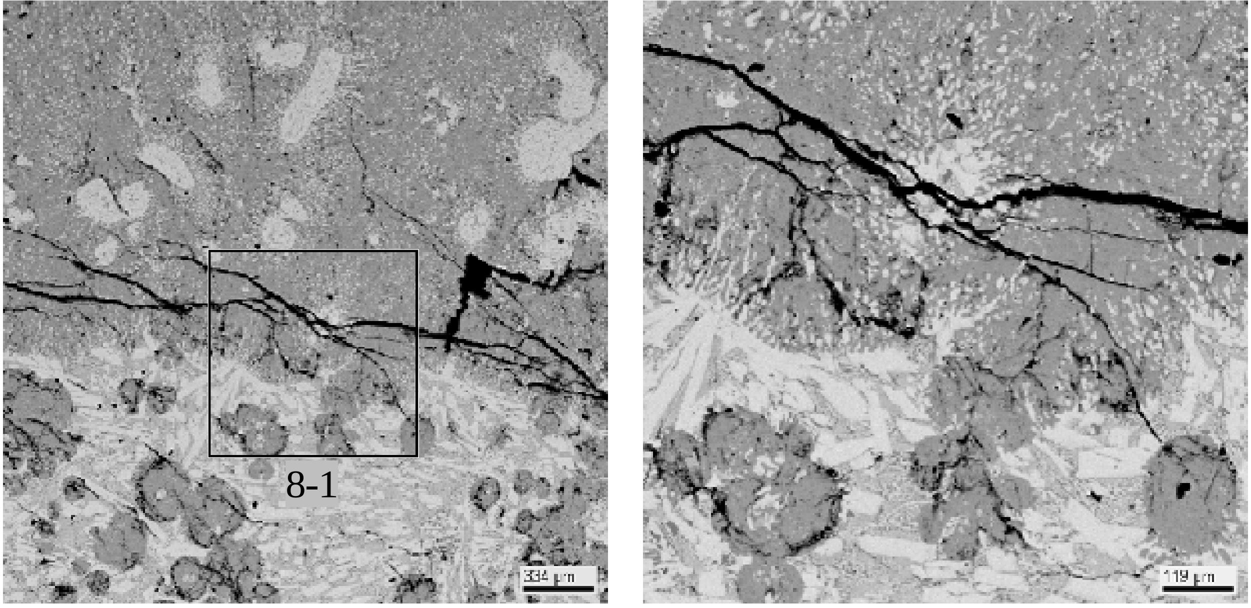

8 8-1

Fig. 3.27. Micrographs of region 8 in the boundary region of the stratified melt, CORD 40

A comparison of composition of the metal-rich globules in the upper layer of the stratified melt (Fig. 3.21, region 2-1-3 and Tab. 3.17, SQ3; Fig. 3.24, regions 5-1-2-1 and 5-1-2-2 and Tab. 3.20, SQ4 and SQ5) with that of regions in the ingot bottom layer (Fig. 3.22, region 3-6, Tab. 3.18, SQ12; Fig. 3.23, region 4, Tab. 3.19, SQ1; Fig. 3.26, Tab. 3.22, SQ1) has shown them to be poorer in iron and richer in uranium.

Region 9 of the ingot (Fig. 3.28) shows microstructure of the periphery region in the oxide-rich upper layer with numerous pores.

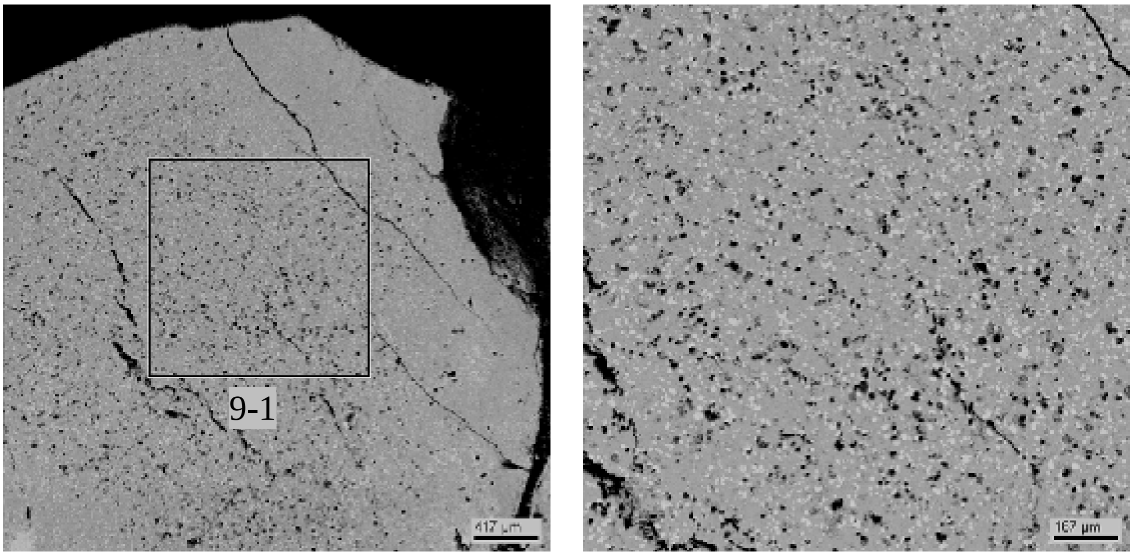

9 9-1 (SQ1)

Fig. 3.28. Micrograph of region 9 in the upper layer peripheral part, CORD 40

Table 3.23. EDX data for region 9

No.		**U**	**Zr**	**Fe**	**~O**
SQ1	mass%	83.57	1.37	-	15.06
	mol.%	26.86	1.15	-	72.00
	mol.% MeO$_x$	95.91	4.09	-	

Region 10 of the ingot (Fig. 3.29) gives an impression of microstructure of the peripheral part of the bottom metal-rich layer that contains the oxide-rich globules.

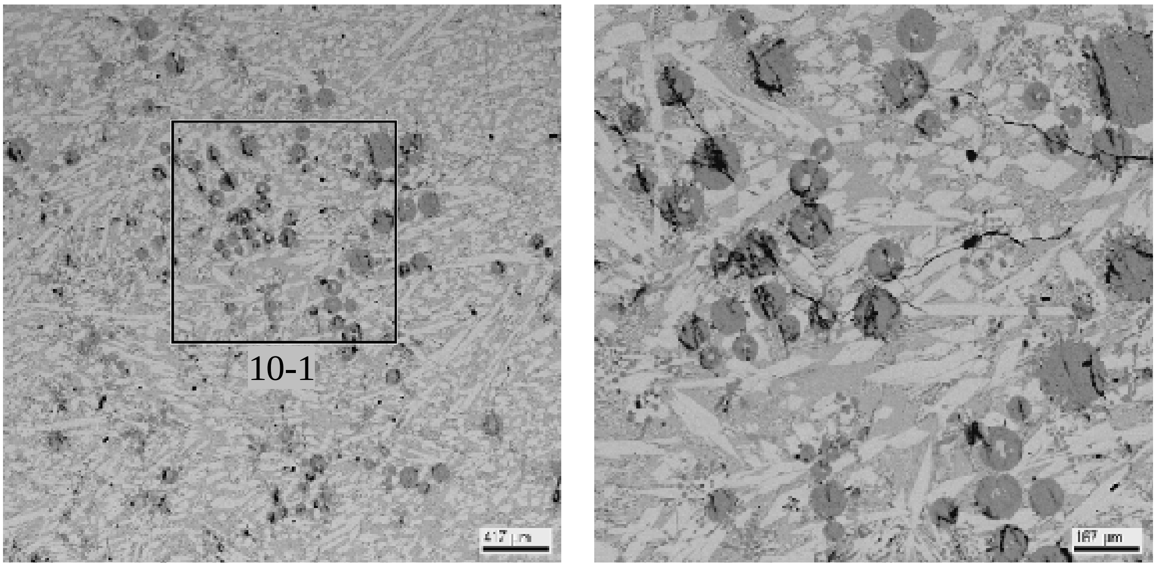

10 (SQ1) 10-1

Fig. 3.29. Microstructures of region 10 in the bottom layer peripheral part, CORD 40

Table 3.24. EDX data for region 10

No.		**U**	**Zr**	**Fe**	**~O**
SQ1	mass%	78.23	0.81	8.05	12.91
	mol.%	25.50	0.69	11.18	62.62
	mol.% MeO_x	68.23	1.84	29.92	

Region 11 demonstrates microstructure of the outer edge of the ingot bottom layer, and regions 12 and 13 – that of the regions located to the ingot bottom (Fig. 3.30). Here, one can see a fairly even distribution of phases, almost complete absence of pores and a reduced content of the dissolved oxygen towards the ingot lower part (Tab. 3.25).

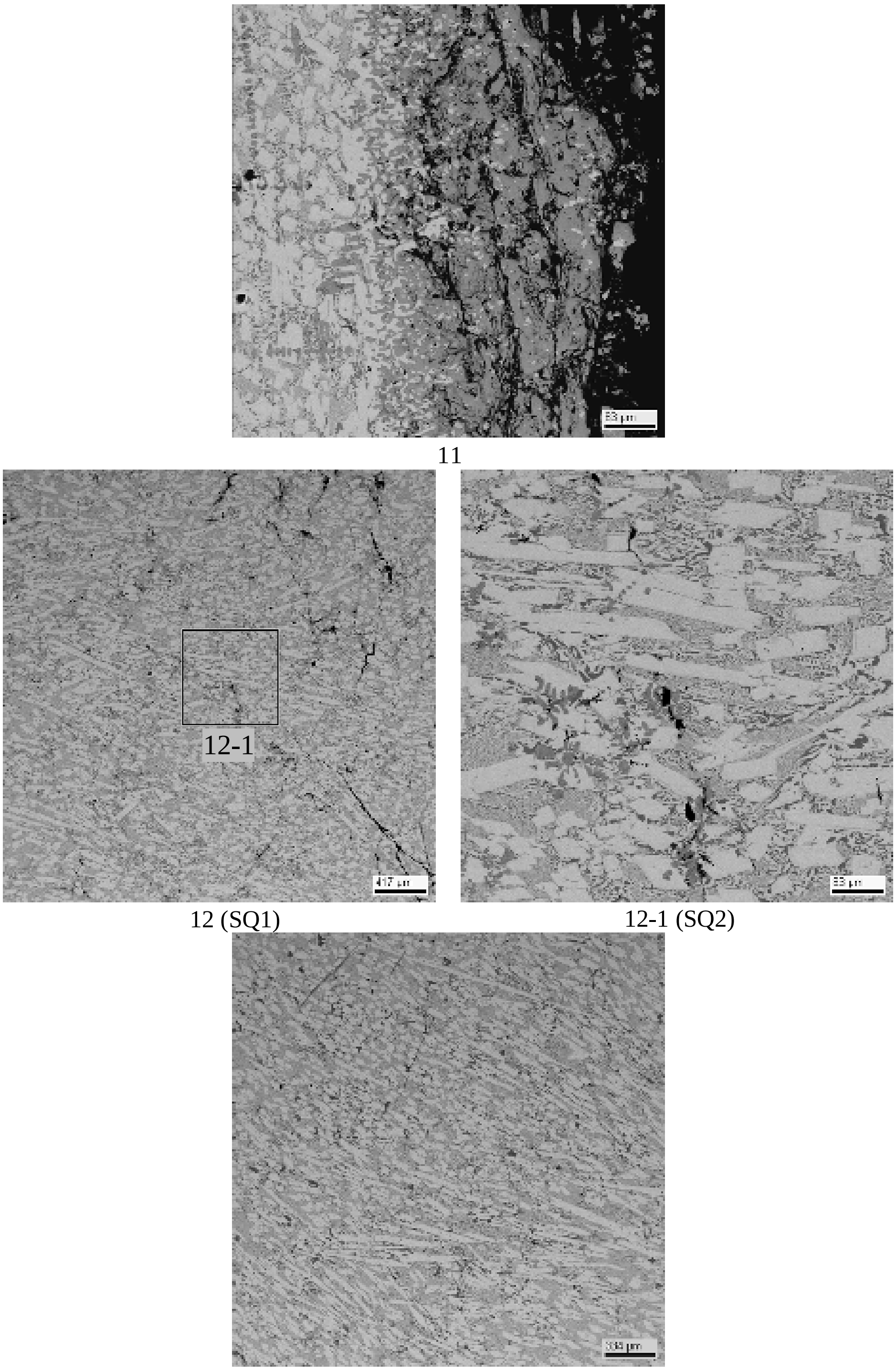

11

12 (SQ1)

12-1 (SQ2)

13 (SQ3)

Fig. 3.30. Micrographs of regions 11, 12 and 13 in the ingot bottom layer, CORD40

Table 3.25. EDX data for regions 12, 13

No.		**U**	**Zr**	**Fe**	**~O**
SQ1	mass%	80.57	0.87	9.07	9.49
	mol.%	30.67	0.87	14.71	53.75
	mol.% MeO_x	66.32	1.87	31.81	
SQ2	mass%	85.22	0.85	9.44	4.49

	mol.%	43.83	1.14	20.7	34.33
	mol.% MeO$_x$	66.74	1.73	31.52	
SQ3	mass%	87.13	0.90	10.10	1.87
	mol.%	54.34	1.47	26.84	17.34
	mol.% MeO$_x$	65.74	1.78	32.48	

Region 14 demonstrates microstructure of the ingot bottom layer. This region contains still less dissolved oxygen (Tab. 3.26), thus maintaining the general tendency.

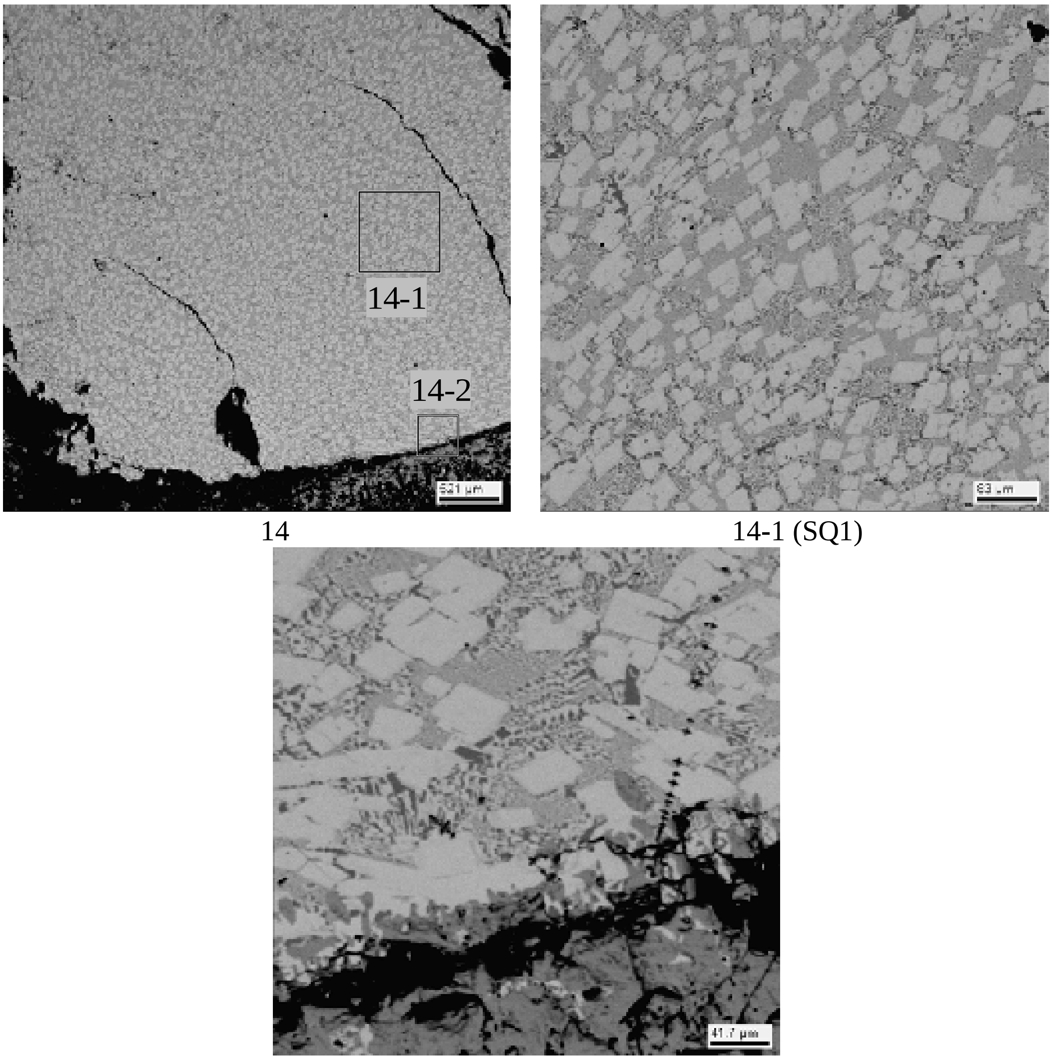

14 14-1 (SQ1)

14-2

Fig. 3.31. Micrographs of region 14 in the lower region of the bottom layer, CORD 40

Table 3.26. EDX data for region 14

No.		U	Zr	Fe	~O
SQ1	mass%	87.65	0.86	9.83	1.65
	mol.%	56.04	1.44	26.79	15.74
	mol.% MeOx	66.51	1.70	31.79	

In general, the bottom layer structure is apparently composed of the U_6Fe, UFe_2 intermetallides (Tab. 3.20, point P2 and Tab. 3.17, points P9, P10) with eutectics between them (Fig. 3.24 and Tab. 3.20, SQ6). The secondary extractions in the form of globules are concentrated at the top of this layer, and this can evidence of their surfacing during crystallization of the matrix phases. The averaged composition of globules from the boundary region of the bottom layer (Fig. 3.22 and Tab.3.18, SQ3, SQ5-8) corresponds to bulk composition of the top layer (Fig. 3.24, region 5-1 and Table 3.20, SQ1).

Tab. 3.27 summarizes the data of SEM/EDX analysis. Bulk compositions of the metallic and oxidic layers were evaluated on the basis of compositions of different regions of the metallic and oxidic ingots.

Table 3.27. Summarized data of SEM/EDX analysis

Liquid	**Studied region**	**U**	**Zr**	**Fe**	**O**
		at.%			
Oxide	**region 6 SQ1 Fig. 3.25**	**90.8**	**3.9**	**5.3**	
	region 5 SQ1 Fig. 3.24	**91.1**	**3.9**	**5.0**	
	average	**90.95**	**3.9**	**5.15**	
	Correction for oxygen*	**41.2**	**1.8**	**2.3**	**54.7**
Oxidic globules in metallic matrix	**region 3 SQ3 Fig. 3.22**	**90.6**	**3.9**	**5.5**	
	region 3 SQ6 Fig. 3.22	**89.9**	**3.0**	**7.1**	
	region 3 SQ7 Fig. 3.22	**92.3**	**3.7**	**4.0**	
	region 3 SQ8 Fig. 3.22	**90.4**	**4.0**	**5.5**	
	average	**90.8**	**3.7**	**5.5**	
Metal (region with globules)	**region 3-6 SQ12 Fig. 3.22**	**70.8**	**1.8**	**27.4**	
	region 4 SQ1 Fig. 3.23	**69.5**	**1.8**	**28.7**	
	region 7 SQ1 Fig. 3.26	**68.9**	**1.6**	**29.5**	
	region 10 SQ1 Fig. 3.29	**68.2**	**1.8**	**29.9**	
	Region with globules, average	**69.3**	**1.8**	**28.9**	
Metal (region without globules)	**region 12 SQ1 Fig. 3.30**	**66.3**	**1.9**	**31.8**	
	region 13 SQ3 Fig. 3.30	**65.7**	**1.8**	**32.5**	
	region 14 SQ1 Fig. 3.31	**66.5**	**1.7**	**31.8**	
	Region without globules, average	**66.2**	**1.8**	**32.0**	
	Correction for oxygen**	**60.8**	**1.7**	**29.4**	**8.1**
Metallic globules in oxidic matrix	**region 5 SQ4 Fig. 3.24**	**76.4**	**3.2**	**20.4**	
	region 5 SQ5 Fig. 3.24	**78.7**	**3.9**	**17.4**	
	region 2 SQ3 Fig. 3.23	**75.3**	**2.4**	**22.3**	
	globules, average	**76.8**	**3.2**	**20.0**	

*) – Oxygen content in the oxidic part was calculated in accordance with the data /2/ on oxygen solubility in the oxidic liquid in the miscibility gap of the U-O system along the 2873 K isotherm (at. %, 43U-57O), and assuming that oxygen is bound only with U.
**) - Oxygen content in the metallic part was calculated in accordance with the CTR data in Tab. 3.28 (0.8 mass %.), and assuming that oxygen is bound only with U.

Compositions of the metallic and oxidic layers given in Tab. 3.27 agree well with the results of XRF (Tab. 3.4) and chemical (Tab. 3.6) analyses.

3.6. Reducing melting of corium samples in carbon crucibles (CTR)

Oxygen content in different regions of the ingot from CORD40 was determined by the method of CTR (carbothermal reduction). The pattern of sampling for the analysis is shown in Fig. 3.8. The method is described in /6/ and is based on determining the change in the sample mass and/or the quantity of the released $CO–CO_2$ at the reduction of oxides in the molten sample with carbon. Tab. 3.28 presents the analysis specifications and the results for CORD40.

Table 3.28. Analysis specifications and results for CORD40

Sample	Carrier gas	Temperature, °C	Sample mass, mg	Exposure time, min	O content, mass%
Oxidic part of ingot (top)	Ar	2500	500	1	7.96, 7.97
Metallic part of ingot (bottom)					0.71; 0.79; 0.86

It is evident from Tab. 3.28 that the oxygen content in the oxidic part is 8.0±0.1 mass % and 0.8±0.07 mass % in the metallic part. These values were used for making up the per-element material balances given in Tabs. 3.5-3.7.

The error of determining oxygen concentration by CTR of samples was less than 3 relative %.

3.7. Differential Thermal Analysis

The method of differential thermal analysis (DTA) was used for T_{sol} determination. A specimen was prepared from the metallic part of the ingot from CORD40 (Fig. 3.8, zone IV). The SETSYS Evolution-2400 analyzer was used for DTA and the SETSOFT 2000 software package for processing the results.

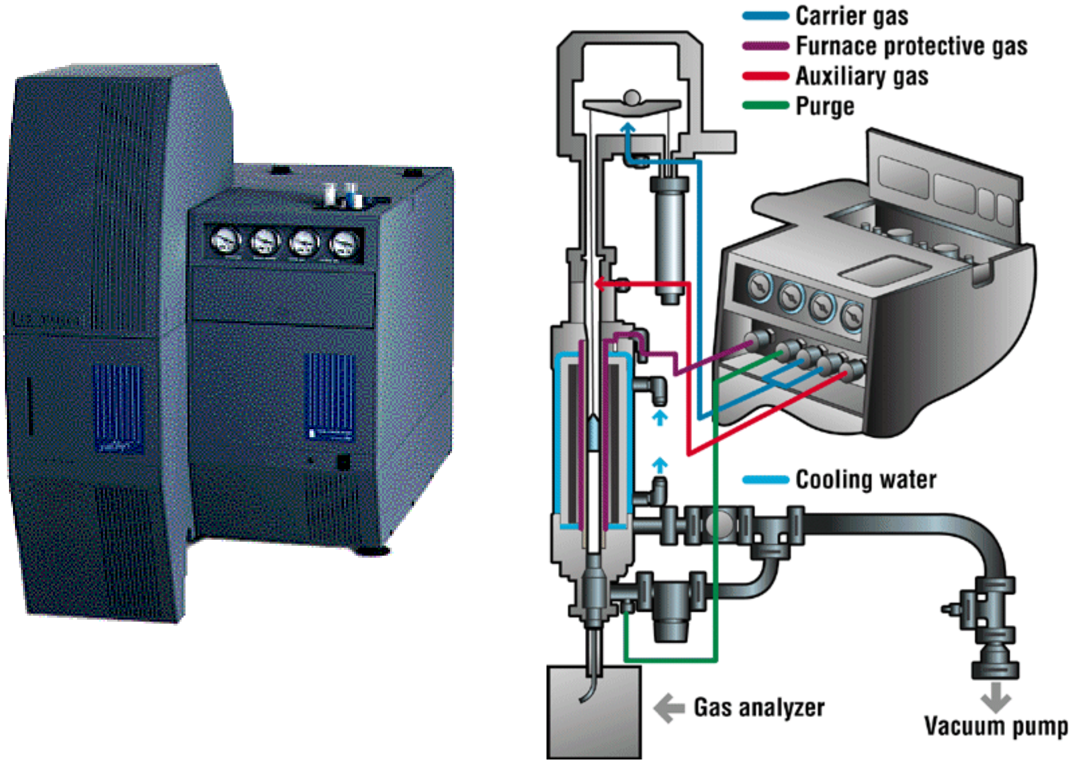

Fig. 3.32. SETSYS Evolution-2400, appearance and schematics

SETSYS Evolution-2400 (Fig.12) covers an extremely wide temperature range from 196° C up to 2400° C and is designed for performing DSC, DTA, TG-DTA and TG-DSC measurements. The accuracy of temperature determination is ±2.5° C. The furnace working space may be either vacuumized, or filled with different gases/mixtures, e.g., air, argon, helium, carbon dioxide. Such a system provides priceless information about the oxidation-sensitive samples.

Analysis specifications:

The mass of the sample was 236.75 mg, and Al_2O_3 was taken as the crucible material. Before the analysis, the measuring cell was vacuumized and then filled with high-purity argon. The heating rate was 5° C/min, and a B-type thermocouple (Pt-30%Pt/Rh-6%Rh) was used. T_{sol} was automatically determined by the thermoanalyzer at the point of tangent crossing the baseline.

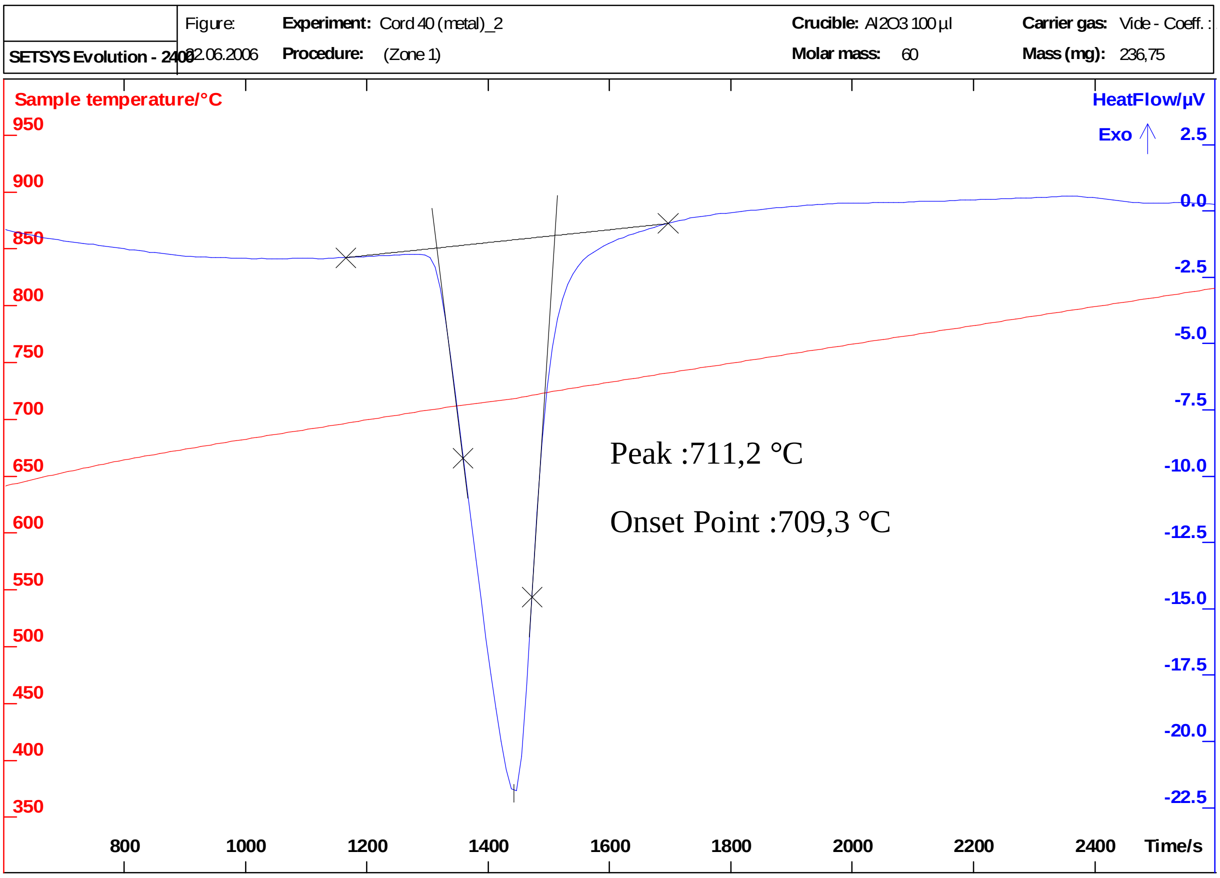

Fig. 3.33. DTA curve at heating

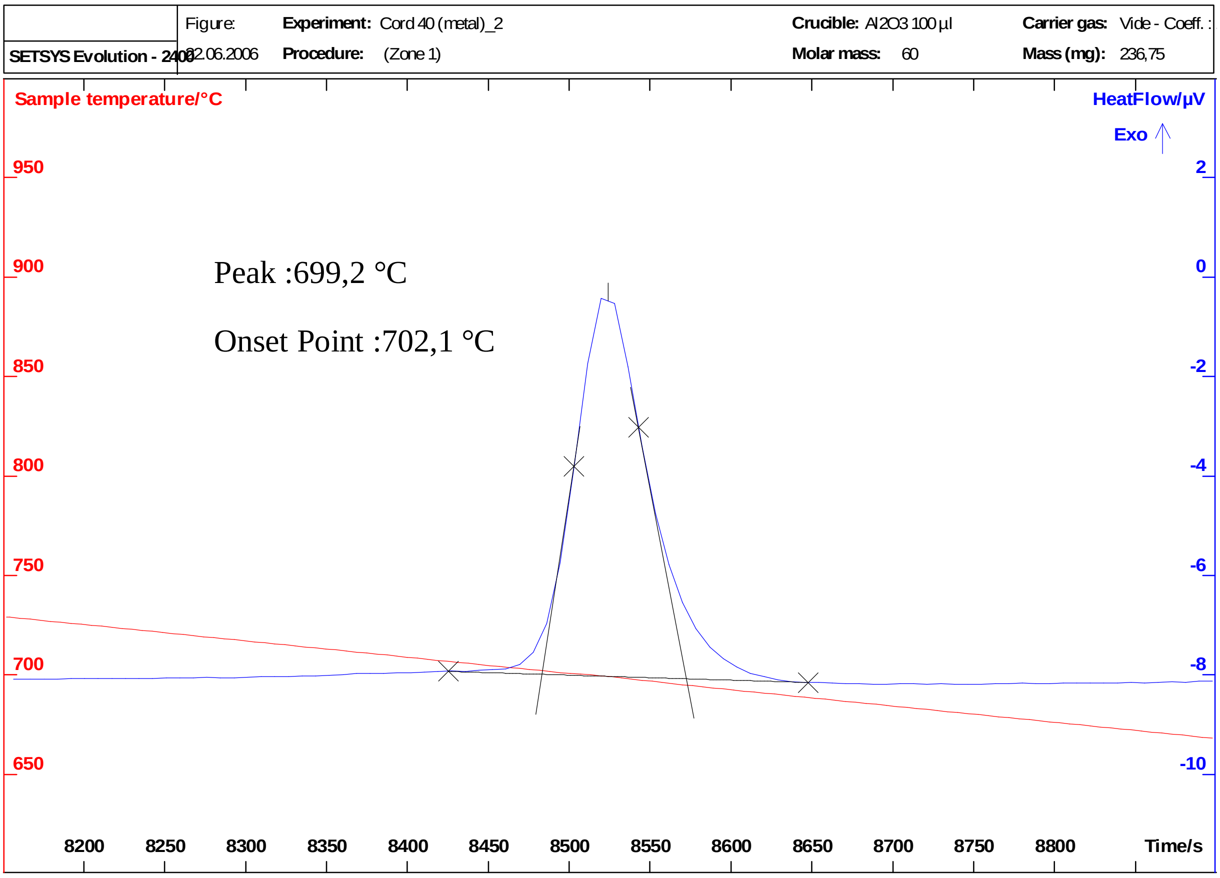

Fig. 3.34. DTA curve at chilling

Fig. 3.33 shows that T_{sol} measured during sample heating was 709°C, i.e., somewhat lower than the eutectic temperature according to /4/. Apparently, this is due to the presence of a small amount of Zr in the eutectic. The measurement at the stage of sample cooling yielded 702° C, which is apparently due to the melt supercooling. It should be noted that no interaction of the liquid phase with the crucible material was observed in the present investigation. Also, it may be supposed that oxygen was either absent or available in very small quantities in the intermetallides that composed the eutectic.

4. Discussion of results

4.1 T_{liq} and T_{sol} measurements

The Project included two tests with the U-Fe-O system that employed identical charge composition (CORD36 and CORD40). In CORD36, the oxidic part was found in the lower part of the ingot. The rounded shape of the UO_2 phase indicates that at crystallization it was surrounded with metallic liquid. Position of the oxidic liquid at the bottom contradicts the data on densities of UO_2 and U. The analysis of thermal condition of the molten pool during the test and morphology of urania grains in the bottom layer suppose that crystallization of the oxidic layer at the pool bottom occurred in the course of the test at a temperature that was lower than the monotectic temperature of the initial composition. In CORD40, the oxidic liquid crystallized in the ingot upper part when heating was switched off at the end of the test.

T_{liq} was measured by the VPA IMCC method /6/. The melt composition in CORD40 differed from the specified one mainly because of a) metallic uranium contamination by zirconium, b) insignificant remains (spillages) of the powdered UO_2, and c) the crust, the composition of which differed from that of the melt by a higher content of refractory phases. However, the crust thickness did not exceed 1 mm. Therefore, composition of the melt which T_{liq} had been measured was calculated on the basis of the crucible charge excluding spillages, aerosols and the crust. Composition of the melt at measuring T_{liq} in CORD36 could not be determined because of the uncontrollable crystallization of the refractory phase at the pool bottom during the test.

T_{sol} was determined by DTA in crucibles made of Al_2O_3. For this analysis, samples were prepared from the metallic part of the ingot from CORD40. The results of the analysis show that there was no interaction of the sample with crucible, and therefore the results of DTA can be acknowledged as reliable. The measured T_{sol} is somewhat lower than the eutectic temperature of the U-Fe system /4/. This may be due to the presence of a small amount of Zr in the sample.

Tab. 4.1 offers a comparison of the measured T_{liq} and T_{sol} with the results of thermodynamic calculations using the GEMINI-2 code and NUCLEA-06 database. Obviously, the measured and calculated temperatures of phase transitions virtually coincide within the margin of error.

Table 4.1. Experimentally obtained and calculated T_{liq} and T_{sol} values

Test	Composition, mass/at. %1)				Experimental		Calculated	
	U	Fe	Zr	O	T_{liq}, K	T_{sol}, K	T_{liq}, K	T_{sol},
CORD40	88.8/60.0	7.5/21.6	2.3/4.0	1.4/14.4	2788	982	2749	990

1) – composition is given taking into account the spillages and debalance.

4.2 Microstructural peculiarities of the crystallized ingot

According to the SEM/EDX data, two layers with different microstructures were found in the ingot from CORD40. The oxygen-rich "oxide-rich" layer is located in the upper part of the ingot and is approximately 3 mm thick. Below is a layer that is approximately 46 mm-thick and is composed presumably of a mixture of intermetallides.

Microstructure of the oxide-rich layer is presented in Fig. 4.1.Microstructure of the upper region of this layer is identical to that observed in the U-UO_2 system. The dark phase is UO_2, and the light-coloured one is U. Notable is high porosity of this layer. Microstructure of the bottom region of this layer is denser, and the dark phase here is UO_2, while the light-coloured one, in the globules as well, is apparently a mixture of U(UFe_2) and U_6Fe.

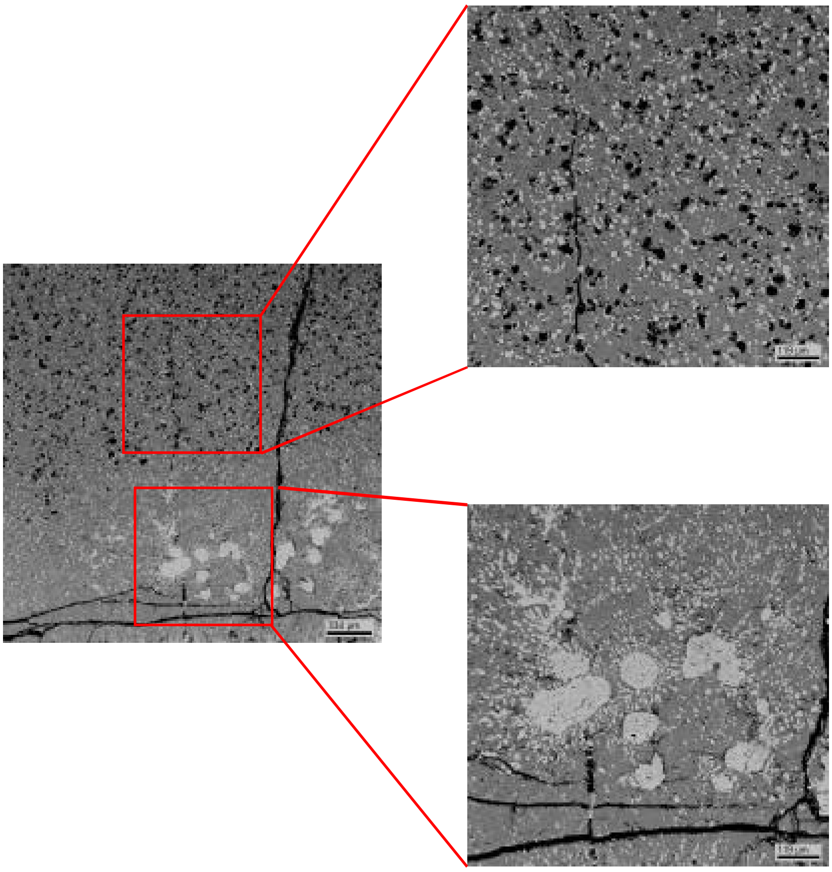

Fig. 4.1 Microstructure of the oxidic layer

Microstructure of the metal-rich layer is also heterogeneous, like that of the oxide-rich one. At the top of this layer, oxidic globules are concentrated, and they are absent in the lower part of the layer.

Microstructures of the top and bottom parts of the metallic layer are compared in Fig. 4.2. The metallic matrix is composed of two intermetallic phases: the light-coloured U_6Fe and dark UFe_2. Also, inclusions of a zirconium-rich intermetallic phase were found as a result of Zr presence in the initial U reagent and $UO_{2.24}$.

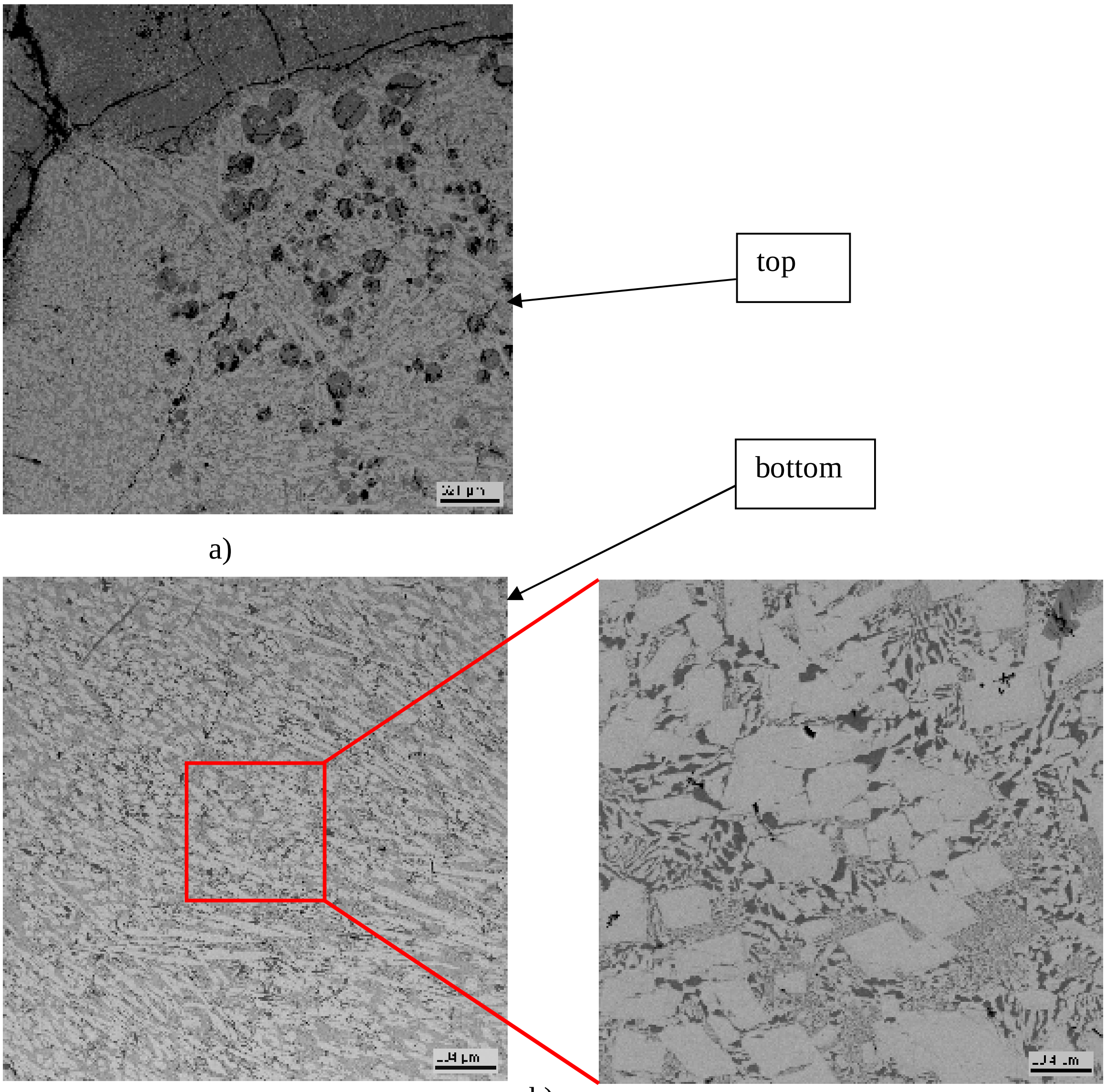

a)

b)

Fig. 4.2 Microstructure of the top and bottom parts of the metallic layer

4.3 Compositions of the oxidic and metallic liquids in the miscibility gap

Determination of the coexisting liquids composition was complicated by a number of factors:

– in presence of a small amount of the light liquid under the IMCC conditions, the heavier liquid surfaces through the layer of the light one, and thus sampling one of the liquids becomes impossible;

– Uneven distribution of components in the top and bottom layers of the crystallized ingot has been recorded. In the top layer, metallic globules are concentrated in its lower part, while in the bottom layer oxidic globules are concentrated at its top.

Formation of oxidic and metallic globules makes determination of the average chemical composition of the layers very uncertain. If the globules result from the secondary isolation during crystallization of each liquid, then they should be included in the bulk composition. It cannot be ruled out that a temperature gradient might have formed at the interphase boundary of two layers, and this, together with convection, could cause instability near the boundary and movements of droplets of the oxidic liquid into the metallic layer and of metallic droplets into the oxidic layer.

According to the results of SEM/EDX analysis, composition of the oxidic globules in the metallic layer is identical to the oxidic layer bulk composition. Obviously, it indicates that the globules have resulted from the secondary isolation during melt crystallization.

When comparing compositions of the analyzed metal-rich and oxide-rich layers (Tab. 4.2), a good agreement between the cationic composition data obtained by different methods for the studied compounds, and the results of thermodynamic calculations using the GEMINI-2 code and NUCLEA-06 database.

The compositions of the top (oxide-rich) and bottom (metal-rich) liquids recommended for the verification purposes were taken from the chemical analysis results, as the per-element material balance made up using the chemical analysis data yielded the least debalance for Fe (Tab. 3.7).

Table 4.2 Results of analyses for CORD40 and thermodynamic calculation of the coexisting phases composition.

Method of analysis	**Element**	**Experimental**		**Calculated**	
		Oxidic liquid	**Metallic liquid**	**Oxidic liquid**	**Metallic liquid**
		Composition, at. % (T= 2823 K)			
ChA	**U**	41.0	64.0	40.0	65.6
XRF		39.5	64.1		
EDX		41.2	60.8		
ChA	**Fe**	2.0	23.5	0.0	27.5
XRF		3.5	24.4		
EDX		2.3	29.4		
ChA	**Zr**	2.3	3.9	1.3	4.8
XRF		3.3	3.0		
EDX		1.8	1.7		
ChA	**O**	54.8	8.5	58.7	2.0
XRF		53.8	8.5		
EDX		54.7	8.1		
Mass fraction, mass%		**6.9**	**93.1**	**14.0**	**86.0**

The data obtained by the analysis of layers of the ingot from CORD40 (Tab. 4.2) show that the content of zirconium in it is comparable with, or sometimes higher than the minimal content of such a component as iron. This circumstance prevents construction of a timeline in the

U–Fe–O ternary system for the given composition at the given temperature. Therefore, the results of the performed investigation are for a four-component system.

5. Conclusion

1. T_{liq} and T_{sol} have been measured for the composition U–Fe–Zr–O (60.0–21.6–4.0–14.4 at. %). The recommended values are: T_{liq}=2788 K, T_{sol}=982 K.

2. Compositions of the liquids that coexist in the miscibility gap of the above-mentioned system at 2873 K have been found to be as follows:

   - the top, oxide-rich liquid, at. %: U–41.0±2, Fe–2±0.2, Zr–2.3±0.3, O–54.8±3;

   - the bottom, metal-rich liquid, at. %: U–64.0±3, Fe–23.5±1.2, Zr–3.9±0.2, O–8.5±0.8.

6. References

1. NUCLEA. Nuclear Thermodynamic Database. Version 2005-01/ Editor B.Cheynet. THERMODATA 2005
2. R.K. Edwards, A.E. Martin. // Thermodynamics. IAEA, Vienna. 1966. V. 2, P. 423.
3. P. Guinet, H. Vaugoyeau, P.L. Blum. // C. R. Acad. Sci. Paris. 1966. T. 263, P. 17-20.
4. Voronov N.M., Voytekhova V.A., Kovalyov I.T. Phase diagram of the urania-zirconia system / In: The structure of alloys of some systems with uranium and thorium (Proceedings of the A.A. Baikov Metallurgical Institute of the Academy of Sciences of the USSR). Moscow. Gosatomizdat Publishers. 1961. P. 467-481 (Rus.).
5. Wriedt H.A. The Fe-O (iron-oxygen) system // Journal of Phase Equilibria. 1991. V. 12. No. 2. P. 170-200.
6. Investigation of binary oxidic systems. System U-Fe-O. ISTC PROJECT # 1950.2. Final report, 2006.
7. T.M. Florence- Analytical methods in the nuclear fuel cycle/ Vienna: JAEA, 1972.
8. V.G. Baranov, Yu.G. Godin, Yu.D. Syedin, V.G. Kosykh et al. Methods of determining O/U ratio in the pre-stoichiometric urania. // Radiokhimiya (Radiochemistry). 1994. V.36. No.3. P. 275-280 (Rus.).
9. GOST 4011-72. Drinking water. Methods for determination of total iron. (Rus.)
10. Sendel E. Methods of metal traces determination by colorimetry. Moscow, Mir Publishers, 1964. (Rus.)
11. Riabchikov D.I., Seniavin M.M. Analytical chemistry of uranium. Moscow, Publishing House of the USSR Academy of Sciences. 1962. (Rus.)
12. Lukianov V.F., Savvin S.B., Nikolskaya I.V. Photometric detection of uranium microquantities using reagent arsenazo III. JACh., V.15, No.3. 1960. (Rus.)
13. S.V. Yelinson, K.I. Petrov. Zirconium. Chemical and physical methods of analysis. Moscow. 1960 (Rus.).
14. Flaschka H., Faran M. // Z. analyt. Chem. 1956. B. 152. H. 6. S. 401.
15. Yu.A. Chernikhov, V.F. Lukianov, E.M. Knyazeva. // JACh. 1959. V.14. P. 207.
16. Losev N.F. Quantitative X-ray fluorescence analysis. Moscow, Nauka Publishers, 1969. (Rus.)
17. Butyrin G.M. Highly porous carbonic materials. Moscow. Khimiya (Chemistry), 1976 (Rus.).
18. Gusarov V.V., Almyashev V.I., Khabensky V.B., Bechta S.V., Granovsky V.S. Components partitioning between the immiscible melts in a nonisothermal system // Fizika I khimiya stekla (Physics and chemistry of glass). 2006. V.32. No.6. P. 875-882 (Rus.).